
CHAPTER 5

Computational Investigation on the Efficiency of Small Molecule Inhibitors Identified from Indian Spices against SARS-CoV-2 Mpro

Computational Investigation on the Efficiency of Small Molecule Inhibitors Identified from Indian Spices against SARS-CoV-2 Mpro

5.1. Abstract:

Recently, small compounds from Indian spices (Carnosol, Arjunglucoside-I, and Rosmanol) have been identified as SARS-CoV-2 main protease (Mpro) inhibitors. The structural dynamics and characteristic features of binding of these small molecules to the SARS-CoV-2 Mpro are not well understood. Here, we have constructed the potential of mean force (PMF) for dissociating Mpro-small molecule inhibitor complexes from the umbrella sampling simulations using the weighted histogram analysis method. Mpro-small molecule inhibitor complexes exhibited relatively higher dissociation energy values than the alpha-ketoamide-Mpro complex (positive control) from the PMF calculations. We found that binding affinity between protein and ligand is higher in Mpro-Arjunglucoside-I complex [$\Delta G_{\text{bind}} = -19.74$ kcal/mol from MM-GBSA and $\Delta G_{\text{bind}} = -9.13$ kcal/mol from MM-PBSA] than in other three SARS CoV-2 small molecule complexes. The MM-GBSA/MM-PBSA calculations revealed that the small molecule inhibitors studied in this work have substantially higher binding affinity for Mpro. We found the residues present in SARS-CoV-2 Mpro's binding pocket contributed the most binding free energy to SARS CoV-2 Mpro-small molecule interactions. Our findings emphasize the structural and binding features of the identified small molecule inhibitors with SARS-CoV-2 Mpro, which could be relevant in developing therapeutic candidates to combat SARS-CoV-2.

5.2. Introduction:

A unique strain of SARS-CoV-2 coronavirus was first detected in Wuhan, a city in China's Hubei Province with a population of 11 million people, in December 2019, following a pneumonia outbreak with no clear reason. The virus has spread to more than 200 countries and territories around the world, and on March 11, 2020, the World Health Organization (WHO) declared it a pandemic [1,2]. There was 288,767,991 laboratory-confirmed coronavirus disease 2019 (COVID 19) infection worldwide as of the 1st of January 2022, with 5,455,634 recorded fatalities. On 16 March 2020, outside of China, the number of cases and deaths surpassed those within the country [3]. SARS-CoV-2 belongs to the coronavirinae

family of single-stranded RNA viruses, divided into four genera: alpha, beta, gamma, and delta [4, 5]. The majority of this family's members are enzootic, with only a few species infecting humans (namely alpha and beta coronaviruses). It also causes minor infections in people, akin to the common cold, and is responsible for 10-30% of upper respiratory tract infections in adults. More severe infections are uncommon, but enteric and neurological diseases may be caused by coronaviruses [6]. A coronavirus might generally take up to two weeks to incubate [7]. Middle East Respiratory Syndrome (MERS), first reported in September 2012 in Saudi Arabia, and severe acute respiratory syndrome (SARS), first reported in 2003 in southern China, are two previous coronavirus outbreaks. MERS infected almost 2,500 people, resulting in more than 850 deaths, while SARS infected over 8,000 people, resulting in approximately 800 deaths. The case fatality rates were 35 percent and 10 percent for these conditions, respectively. SARS-CoV-2 is a novel coronavirus strain that has never been found in humans before. Although the incubation period of this strain is currently unknown, the US Centers for Disease Control and Prevention advise that symptoms can appear as soon as 2 days after exposure and as late as 14 days after exposure [7]. The current pandemic predicament has prompted the scientific community to conduct a time-sensitive quest for effective antiviral therapy techniques. Computational techniques are one of the most extensively used approaches for detecting potential therapeutic agents. Several drug like or lead-like candidates have been found or repurposed against the SARS-CoV-2 drug target proteins. It is well known that viruses that cause human disease encode one or more proteases, which are essential components of the viral life cycle.

Proteases are the ideal therapeutic targets for viral infections because they cleave the viral polyprotein, allowing the virus to continue to replicate [8, 9]. In cases where the virus has evolved mutational resistance, protease inhibitors have been employed along with the drug treatment. Protease inhibitors were utilized in conjunction with nucleoside reverse transcriptase to treat viral disorders such as acquired immunodeficiency syndrome, and this combination therapy method to overcome drug resistance was successful. The SARS-CoV-2 replicase enzyme encodes pp1a and pp1ab polyproteins, which create all functional polypeptide units required for replication and transcription. The catalytic cleavage action of 3CLpro releases polypeptides at different subsites of polyproteins. For all coronaviruses, this cleavage mechanism is retained in 3CLpro. The protease 3CLpro has been identified as a possible therapeutic target for COVID-19 therapy due to its important role in viral replication and the lack of a similar homolog in humans [10-22]. SARS-CoV-2 Mpro plays a critical function in the processing of polyproteins transcribed from viral RNA, and therefore this protease is viewed as a key to critical

survival and development. Despite its potential, the search for 3CLpro inhibitors that could be used to treat COVID-19 has so far been unsuccessful. For the COVID-19 treatment, many computational studies have focused on currently available antiviral medicines [23-33] targeting the viral replication process. Computer-aided drug discovery technologies have developed as crucial and powerful tools in the drug development process over the last decade. They have been used to uncover protein inhibitors and analyze protein-drug and protein-protein interactions. Because turning a candidate drug into an approved drug is a time-consuming and costly process. A combination of computer methodologies such as virtual screening, docking, MD simulation, and binding free energy evaluation can help identify potential drug candidates from compound libraries. Many *in silico* studies have been conducted to identify potential SARS-CoV-2 inhibitors. In one of the studies, using the virtual screening method, small chemical molecules (Carnosol (CAN), Arjunglucoside-I (ARJ), and Rosmanol (ROS)) from Indian spices have been identified, and the results showed that they have the capacity to inhibit SARS-CoV-2 Mpro and may have antiviral properties against nCoV [34]. Furthermore, anti-carcinogenic activities have been reported for these small chemical compounds [36-37]. However, more research into these inhibitors' effects on SARS-CoV-2 Mpro is needed before clinical trials may be undertaken. In this study, we used the potential of the mean force method to show these small molecule inhibitors' likely binding (unbinding) approach with SARS-CoV-2 Mpro during the formation (dissociation) of the corresponding complex in terms of free energy as a function of the reaction coordinate.

We employed molecular docking and MD simulations to study the binding interaction of the small molecule inhibitors with SARS-CoV-2 Mpro. These small molecule inhibitors SARS-CoV-2 Mpro complexes were subjected to binding free energy calculations and a per-residue energy breakdown study. The molecular mechanics Poisson Boltzmann surface area (MM-PBSA) and the molecular mechanics Generalized Borne Surface area (MM-GBSA) approaches were applied to compute the binding free energy and identify the residues of Mpro involved in interaction with the small molecule inhibitors. The MM-GBSA/MM-PBSA calculations exhibited that the small molecule inhibitors considered in this study showed a marked binding affinity with Mpro compared to the positive control (P3-Capped alpha-ketoamide inhibitor 40 (AKA)). In this study, we have considered AKA a positive control because recently, AKA was reported to be more potent than anti-HIV retroviral drugs such as lopinavir and darunavir [21]. The contribution of each residue to the binding free energy was examined to gain a better knowledge of the binding features of Mpro-small molecule inhibitor complexes. Our findings emphasize

the structural and binding features of the identified small molecule inhibitors with SARS-CoV-2 Mpro, which could be relevant in developing therapeutic candidates to combat SARS-CoV-2.

5.3. Materials and methods:

5.3.1. Initial structure preparation and molecular docking.

5.3.1.1. Preparation of receptor (SARS-CoV-2 Mpro).

The receptor molecule for docking purpose was the 3-D structure of the SARS-CoV-2 Mpro with unliganded active site (PDB ID: 6y84 with resolution of 1.39 Å) which was obtained from the Research Collaboratory for Structural Bioinformatics Protein Data bank (RCSB-PDB) (www.rcsb.org) [38].

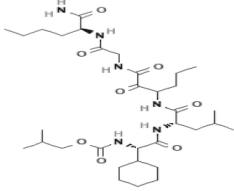
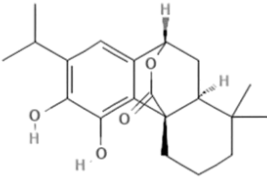
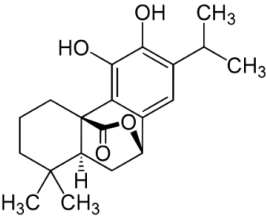
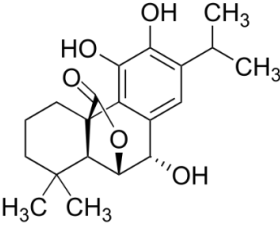
5.3.1.2. Preparation of ligands.

The Chemical structures of the ligands, namely (i) Alpha-ketoamide (positive control) (ii) Arjunglucoside-I (iii) Carnosol and (iv) Rosmanol in SDF format was retrieved from PubChem online server details are summarized in (Table 5.1). The Open bable server was used to convert the SDF format of these small molecules to PDB format.

5.3.1.3. Preparation of the SARS-CoV-2 Mpro-ligand complexes.

The receptor molecule (SARS-CoV-2 Mpro) retrieved from Protein Data Bank was then docked to the ligands (Alpha-ketoamide, Arjunglucoside-I, Carnosol and Rosmanol) using the PatchDock/Firedock [39] online docking server. PatchDock employs a structure-based molecular docking technique. The PatchDock algorithm splits the protein molecules' Connolly dot surface representation into three classes: convex, concave, and flat patches [41,42]. The candidate transformations were then created by combining complementary patches.

Table 5.1. Details of the small molecule inhibitors obtained from Pubchem database.

S.no.	Name of small molecule	PubChem-ID	Structure
1.	Alpha-ketoamide (AKA)	6481510	
2.	Arjunglucoside-I (ARJ)	14658050	
3.	Carnosol (CAN)	442009	
4.	Rosmanol (ROS)	13966122	

A scoring function that includes both the atomic desolvation energy and geometric fit is also applied to evaluate each candidate transformation. First, RMSD clustering is used by the candidate solutions to eliminate redundant Solution. The PDB coordinate files of protein and ligand molecules are used as input parameters for docking. In the PatchDock analysis, three key processes are followed: (i) surface patch matching, (ii) molecular shape representation, and (iii) filtering and scoring. From the PatchDock server, many resulting docked model complexes were generated for the four SARS-CoV-2 Mpro-ligand complex system. In all the four complex systems, the initial complex structure was

chosen based on its atomic contact energy, geometric surface, and geometric shape complementarity score. Using UCSF Chimera [42], the complex structure was examined, the ligand and receptor sections were separated, and their co-ordinates were stored in mol2 and PDB formats respectively. Using the antechamber protocol, the selected solution structure was further curated in xleap. This includes bcc charge addition, frmod file generation, and PDB formats respectively. Using the antechamber protocol, the selected solution structure was further curated in xleap. This includes bcc charge addition, frmod file generation, and complex system in explicit and implicit solvation. The topology and coordinate files for each of the four complex systems were then prepared individually.

5.3.2. MD simulation of receptor-ligand complexes.

The initial coordinate and topology file for the separated receptor and ligands structures for all four complexes were produced using the AMBER ff99SB force field and the Leap module of the AMBER 14 software package. The receptor and its ligand were then loaded together, and the coordinate and topology files of the loaded receptor-ligand complex were created using the Leap module in both implicit and explicit environments. The loaded system was solvated in all directions with the TIP3P [43] water model with a solvent buffer of 10 Å. The complex's charge was then neutralised by the addition of the appropriate number of counter ions. The four receptor-ligand complexes were then subjected to energy minimization in two phases using the AMBER 14 software package, with the first 500 steps of steepest descents minimization (while preserving restraints over the solute) and the second 500 steps of conjugate gradient minimization (devoid of restraints on the solute).

The MD experiment was carried out according to a standard technique, which included heating dynamics, density, equilibration, and production dynamics. We used an energy minimized receptor-ligand system as the starting structure for ensuing MD steps. The density procedure was performed after the individual receptor-ligand system was gradually heated from 0-300 K in constant volume (NVT) conditions. Later the system was equilibrated for 1 ns in NPT conditions (300 K and 1 atm pressure). The density, temperature, pressure, and energy graphs were plotted and examined to guarantee the system's successful equilibration. Then, using the Particle Mesh Ewald (PME) method [44,45], we ran a 10 ns MD production run for the equilibrated structure of the receptor-ligand system with a time step of 2 fs. During the simulation, a cut-off of 8 Å was used to tackle nonbonding interactions (short-range electrostatic as well as van der Waals interactions), whereas the PME

approach was used to treat long-range electrostatic interactions. The SHAKE algorithm [46] was used to constrain all of the bonds in the system. The Berendsen weak coupling algorithm [47] was used to maintain the pressure and temperature (0.5 ps of heat bath and 0.2 ps of pressure relaxation) constant throughout the simulation.

After the 10 ns of production dynamics of the four receptor-ligand complexes were completed, the RMSD clustering algorithm was used to extract the lowest energy conformer of each individual complex from the densely populated clusters, followed by the measurement of the centre of mass(es) (CoM) distance between the receptor and the ligand in the complex structure. The extracted structures of each of the four complexes were then used as the starting point for PMF [48] analysis.

5.3.3. *PMF calculation.*

AMBER software was used to create PMF for the four small molecule inhibitor complexes of SARS-CoV-2 Mpro utilizing Alan Grossfield's Weighted Histogram Analysis Method (WHAM) [49] employing umbrella sampling (US) [50] simulations. PMF is used to determine free energy along a certain reaction coordinate, and this free energy profile aids in the identification of transition states, intermediates, and relative end point stabilities. However, simply running the MD simulation to generate free energy along the reaction coordinate will not generate accurate PMF because the energy barrier of interest is many times the size of $k_B T$, so the MD simulation will either stay in the local minimum it started in or cross to different minima, rarely sampling the transition state. US sampling strategy is used with WHAM [39] which helps in attaining the transition states of the interest samples. The reaction coordinates for the four small molecule inhibitor complexes of SARS-CoV-2 Mpro were divided into series of windows by the US, and then restraints were given to the samples to keep them close to the center of window, ensuring that the end points overlapped. The Hamiltonian was then augmented with biasing potentials to limit the molecular system to certain regions of phase space. The biasing potential is typically a harmonic potential that keeps the system in the reaction path close to a specified value. This was carried out in several windows throughout the reaction path. Equilibrium simulations were run in each window, and the biased probability distribution (histogram) was calculated. The optimal free energy constants for the combined simulations are then determined using the WHAM.

The PMF calculation for studying the degree of association between the corresponding small molecule

inhibitor and the SARS-CoV-2 Mpro was done by increasing and decreasing the CoMs distance between the corresponding small molecule inhibitor and the SARS-CoV-2 Mpro in two separate directions from the starting point. The CoMs distance between the small molecule inhibitor and the SARS-CoV-2 Mpro was altered from 8 Å to 25 Å in all four small molecule inhibitor complexes of SARS-CoV-2 Mpro, spanning diverse configurations. Because the buffer of water is 10 Å out of solute, it is expected that a component of the complex structure will emerge out of the solvation box for bigger distances of separation (more than 15 Å) of the ligand and receptor units in the complex. So, at a wider umbrella sampling distance (for each window of the US simulation), we took the solute (complex) and resolvated it with TIP3P water molecules with a solvent buffer of 10 Å enclosing the complex from all sides, as well as neutralised the system with counter ions. Prior to the US simulation, we ensured that the complex system's periodic boundary conditions and equilibration were in place. The system was run for 5 ns of MD simulation with harmonic potentials at each distance of US window to keep the CoM distance between the two monomeric units near the required values. For all four small molecule inhibitor complexes of SARS-CoV-2 Mpro, we calculated the PMF as a function of reaction coordinate.

5.3.4. MD simulation of the structure with the lowest energy of the SARS-CoV-2 Mpro-small molecule inhibitor complexes.

A structure with the lowest potential energy was chosen from the ensemble of related SARS-CoV-2 Mpro small molecule inhibitor complex structures at the reaction co-ordinate corresponding to the minimum PMF values and then subjected to MD simulation to examine its prominent structural features. Then the same conventional approach was utilized for minimization, heating, density, equilibration, and production dynamics of lowest energy structure of the SARS-CoV-2 Mpro- small molecule inhibitor complexes, but with a 50 ns modification in the duration of the production run. The PTRAJ (short for Process TRAJectory) and CPPTRAJ (a rewriting of PTRAJ in C++) modules [51] of AMBER 14 Tools were used to evaluate the MD trajectories for the four complexes. To assess the convergence of the four complex systems, we looked at the RMSDs for the ligand and complex, using the corresponding initial structure as a reference. We also calculated the RMSFs and Rg to examine the four complexes' flexibility and size. In addition, for each of the four complexes, intermolecular hydrogen bond analysis were carried out to see how the complex's stability is altered during MD simulation.

5.3.5. Binding free energy (BFE) analyses for the four SARS-CoV-2 Mpro- small molecule inhibitor complexes.

The four SARS-CoV-2 Mpro-small molecule inhibitor complexes were subjected to BFE investigations. The MMPBSA.py script [52] of the AMBER 14 suite was used to calculate the relative BFE and per-residue energy decomposition (PRED) of the interface residues of the four complexes in this work. The Molecular Mechanics-Poisson Boltzmann Surface Area (MM-PBSA) and Molecular Mechanics-Generalized Borne Surface Area (MM-GBSA) algorithms are used to create this script. To determine the binding free energy (ΔG_{bind}) and comprehend the roles of electrostatic and van der Waals terms in the formation of complexes, the MM-PBSA/GBSA methods were used.

The equations (1-6) show the formulas for computing the BFE and their decomposed energy components. The free energy difference between the bound state complex (G_{complex}) and the free state individuals of receptor (G_{receptor}) and ligand (G_{ligand}) is represented by the total BFE (ΔG_{bind}). ΔG_{bind} can be divided into the enthalpy (ΔH) and the entropy ($-T\Delta S$) using the second law of thermodynamics. The enthalpies were determined with a low computing effort using Poisson–Boltzmann or Generalized-Born surface area continuum solvation (MM-PBSA/MM-GBSA) method [53,54], and the entropy was evaluated using normal mode (nmode) analysis [55,56]. After calculating MM-PBSA/MM-GBSA using all of the trajectories, three components of the individual four complexes were analysed: (i) ligand (ii) receptor (iii) complex. Many recent in-silico investigations [57-63] have employed the methodologies and protocols that we evaluated in this study to estimate the binding free energy.

BFE for the four complex systems were calculated using **Equation (1)**

$$\Delta G_{\text{binding}} = \Delta G_{\text{complex}} - [\Delta G_{\text{receptor}} + \Delta G_{\text{ligand}}] \dots\dots\dots (1)$$

where, $\Delta G_{\text{binding}}$ is the total binding free energy.

Thermodynamically,

$$\Delta G = \Delta H - T\Delta S \dots\dots\dots (2)$$

$$\Delta G = \Delta E_{\text{MM}} + \Delta G_{\text{sol}} - T\Delta S \dots\dots\dots (3)$$

$$\Delta E_{\text{MM}} = \Delta E_{\text{int}} + \Delta E_{\text{ele}} + \Delta E_{\text{vdw}} \dots\dots\dots (4)$$

and

$$\Delta G_{\text{sol}} = \Delta E_{\text{PB/GB}} + \Delta E_{\text{SURF}} \quad \dots\dots\dots (5)$$

$$\Delta E_{\text{SURF}} = E_{\text{NP}} + E_{\text{dis}} \quad \dots\dots\dots (6)$$

5.3.6. *Enthalpy calculations with MM-GBSA/PBSA.*

$\Delta G_{\text{complex}}$, $\Delta G_{\text{receptor}}$ and ΔG_{ligand} indicate free energy contributions from small molecule inhibitor-SARS-CoV-2 Mpro (complex), SARS-CoV-2 Mpro (receptor), and small molecule inhibitor (ligand) for the four complex systems, as given in **Equation 1**.

As stated in **Equation 3**, the enthalpy portion is derived by adding the change in molecular dynamics energy (ΔE_{MM}) and the solvation free energy (ΔG_{sol}). ΔE_{MM} is composed of internal energy (ΔE_{int}) (bond, angle and dihedral energies), electrostatic interaction (ΔE_{ele}) and vander Waals interaction (ΔE_{vdw}). The solvation free energy is divided into polar ($\Delta E_{\text{PB/GB}}$) and non-polar (ΔE_{SURF}) contribution **Equation 5**. $\Delta E_{\text{PB/GB}}$ is derived using Poisson-Boltzmann/Generalized-Boltzmann models and ΔE_{SURF} is the sum of non-polar contribution calculated by PB (E_{NP}) and dispersion energy (E_{dis}) using Solvent accessibility surface area (SASA).

5.3.7. *Conformational entropy calculation based on nmode.*

The normal mode analysis [55,56] and the python-based mmpbsa py nbnmode tool were used to compute the conformational entropy (TAS) during the interaction of receptor and ligand units in the four complexes. The normal modes for the complex, receptor, and ligand were determined and then averaged to obtain a binding entropy estimate in this study. The PRED analysis calculates the energy contribution of each protein residue by examining its molecular interactions across all of the complex's residues.

The methods and their objectives carried out in this work have been briefed in the form of flowchart in **Figure 5.1**.

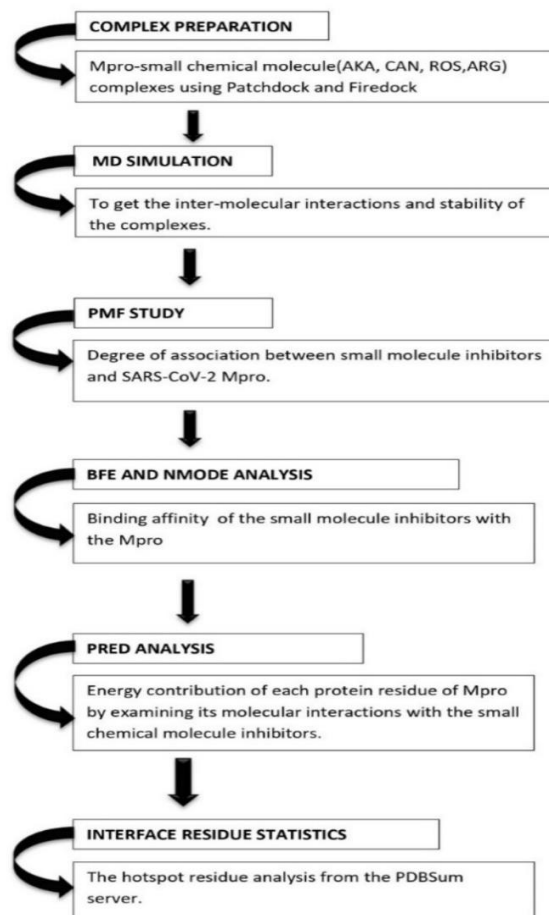


Figure 5.1. Flowchart representing the methods and protocols followed in this work

5.4. Results and Discussions:

5.4.1. PMF profile of SARS-CoV-2 Mpro-ligand complexes.

To analyse the unbinding pathway of each of these small molecule inhibitors and the positive control AKA from the SARS-CoV-2 Mpro, a PMF study was done by combining MD simulations with the umbrella sampling (US) method [50]. The equilibrated complex structure of Mpro –AKA/other small molecule inhibitors (ARJ, CAN, ROS) were chosen as the starting structure for the US simulation. We plotted the density, temperature, potential energy, kinetic energy, and total energy of the AKA/small molecules-SARS-CoV-2 Mpro complex as a function of simulation time to ensure that our NPT simulation algorithm was correct shown in **Figure 5.2, 5.3, 5.4 and 5.5.**

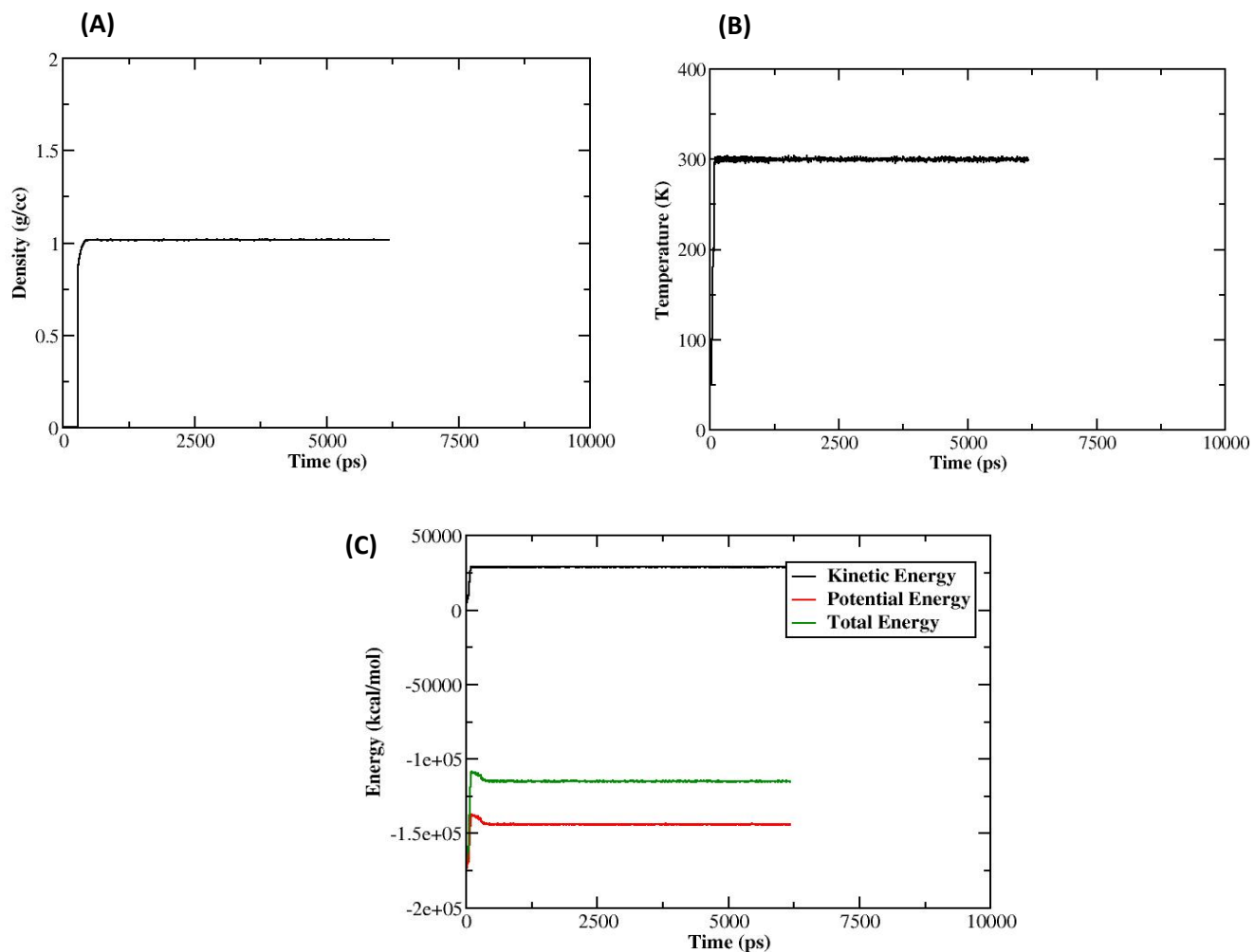


Figure 5.2. (A) Density, (B) Temperature, and (C) Energy plots of SARS-CoV-2-Alpha-ketomaide complex system as a function of simulation time.

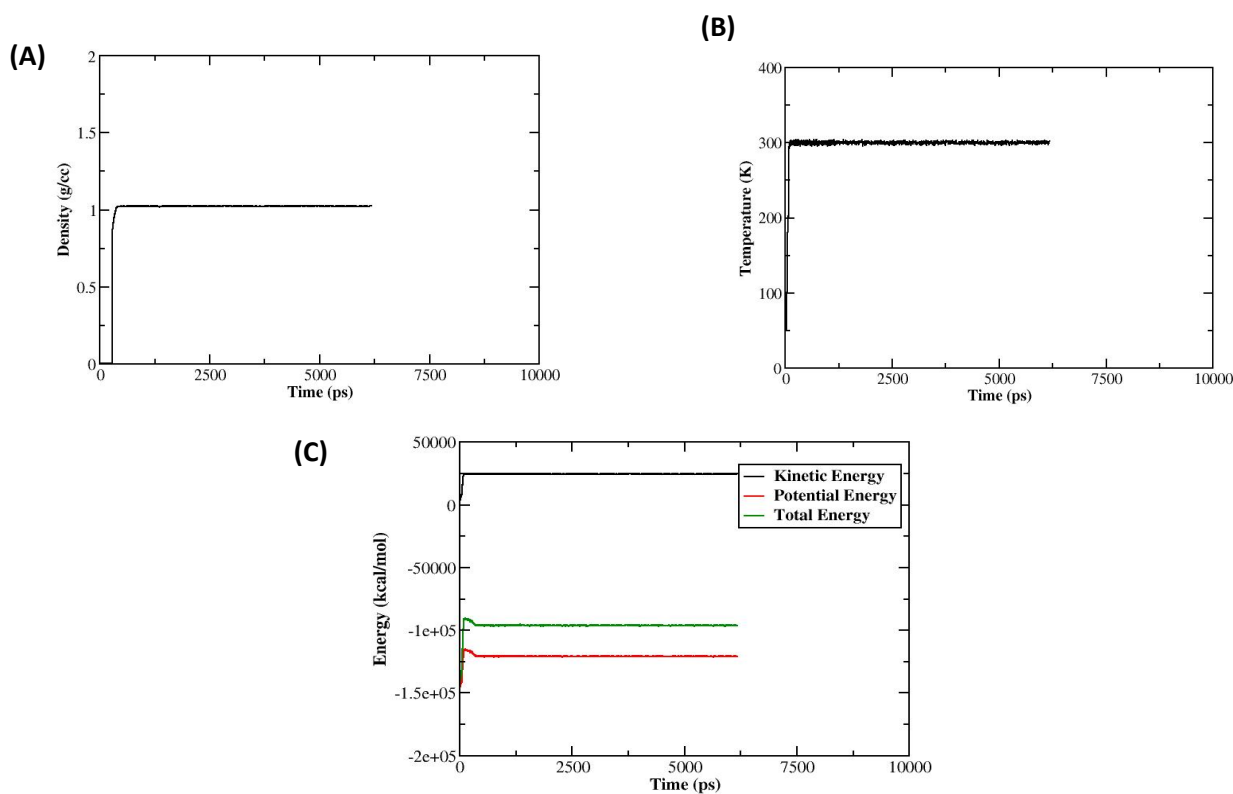


Figure 5.3. (A) Density, (B) Temperature, and (C) Energy plots of SARS-CoV-2-Arjunglucoside-I complex system as a function of simulation time.

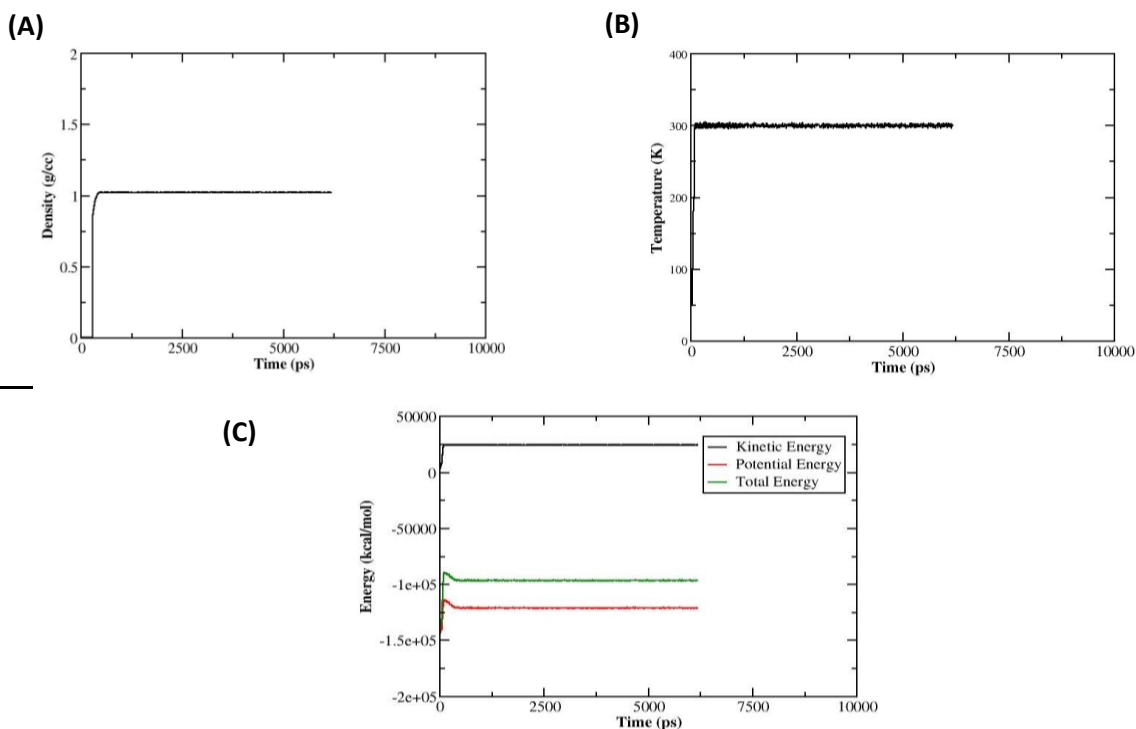


Figure 5.4. (A) Density, (B) Temperature, and (C) Energy plots of SARS-CoV-2-Carnosol complex system as a function of simulation time

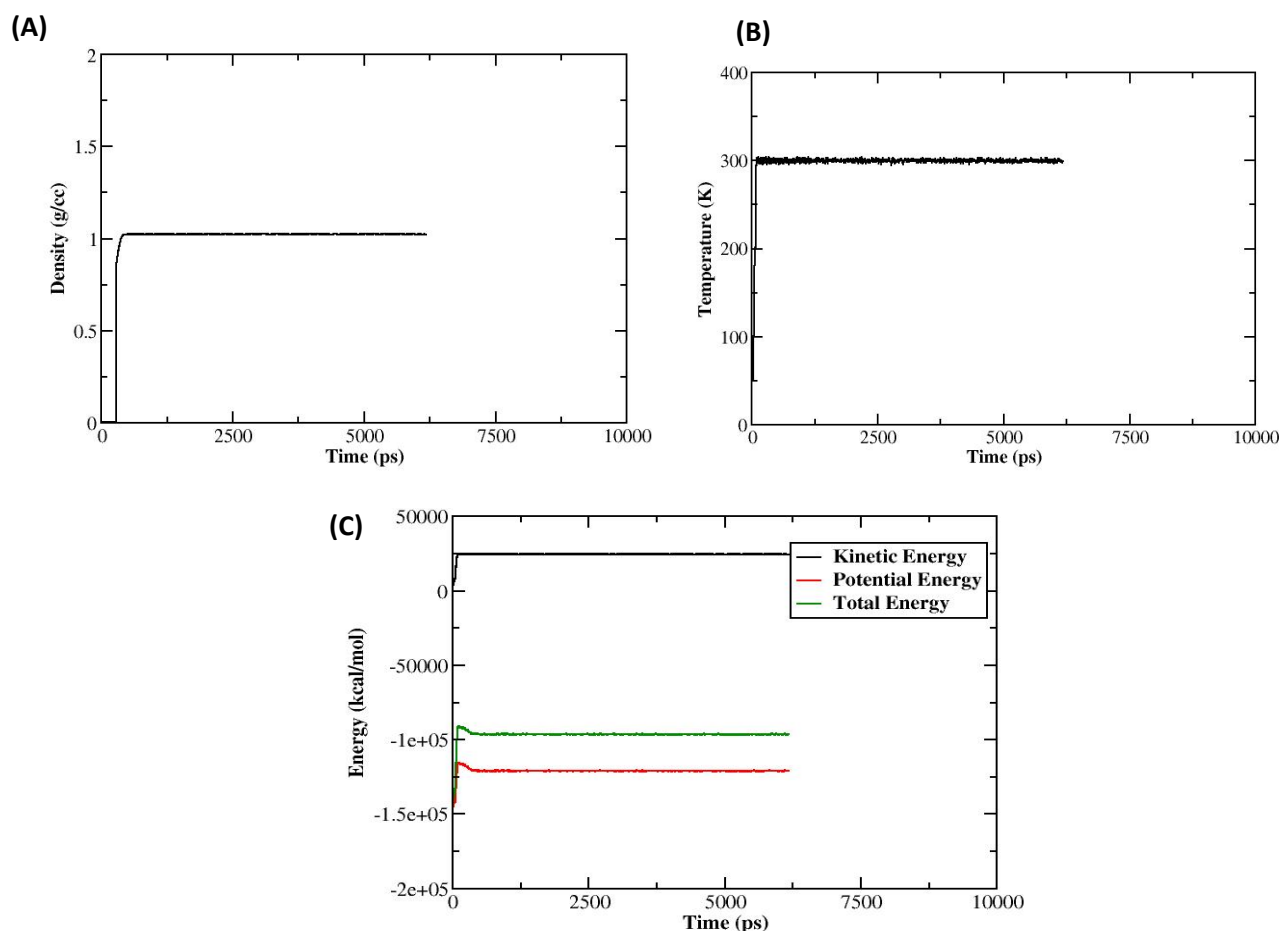


Figure 5.5. (A) Density, (B) Temperature, and (C) Energy plots of SARS-CoV-2-Rosmanol complex system as a function of simulation time.

Figure 5.6 shows the PMF profile for Mpro – AKA/ small molecules (ARJ, CAN, ROS) in water at normal temperature as a function of reaction coordinate. The reaction co-ordinate is defined as the distance between the AKA/small molecules and SARS-CoV-2 Mpro centres of mass. For the Mpro – AKA/ small molecules, 5 ns simulations were performed for each window to assure the sampling convergence of US simulations. And, as shown in **Figure 5.7**, the convergence of PMF was evaluated after each nanosecond of simulations. The strategy that we have employed to check the convergence of PMF was the standard one and used in earlier works [63].

The PMF depths from the US simulation of SARS-CoV-2 Mpro-small molecule systems were found to be larger than those from the SARS-CoV-2 Mpro-AKA complex system (**Figure 5.6**), indicating a deeper energy potential depth and hence a longer residence period of the small molecules in the SARS-CoV-2 Mpro binding pocket.

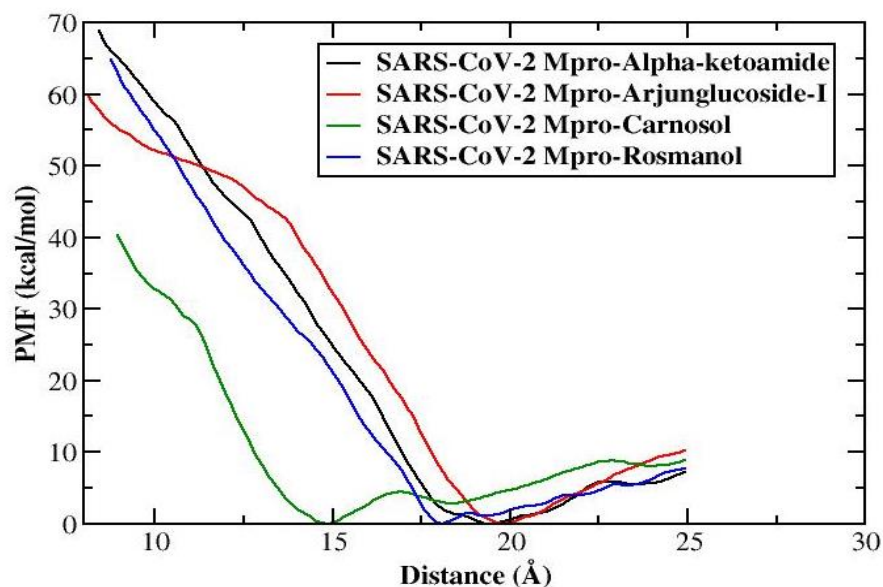


Figure 5.6. Potential of Mean Force for the association and dissociation of the SARS-CoV-2 Mpro-small molecule complexes.

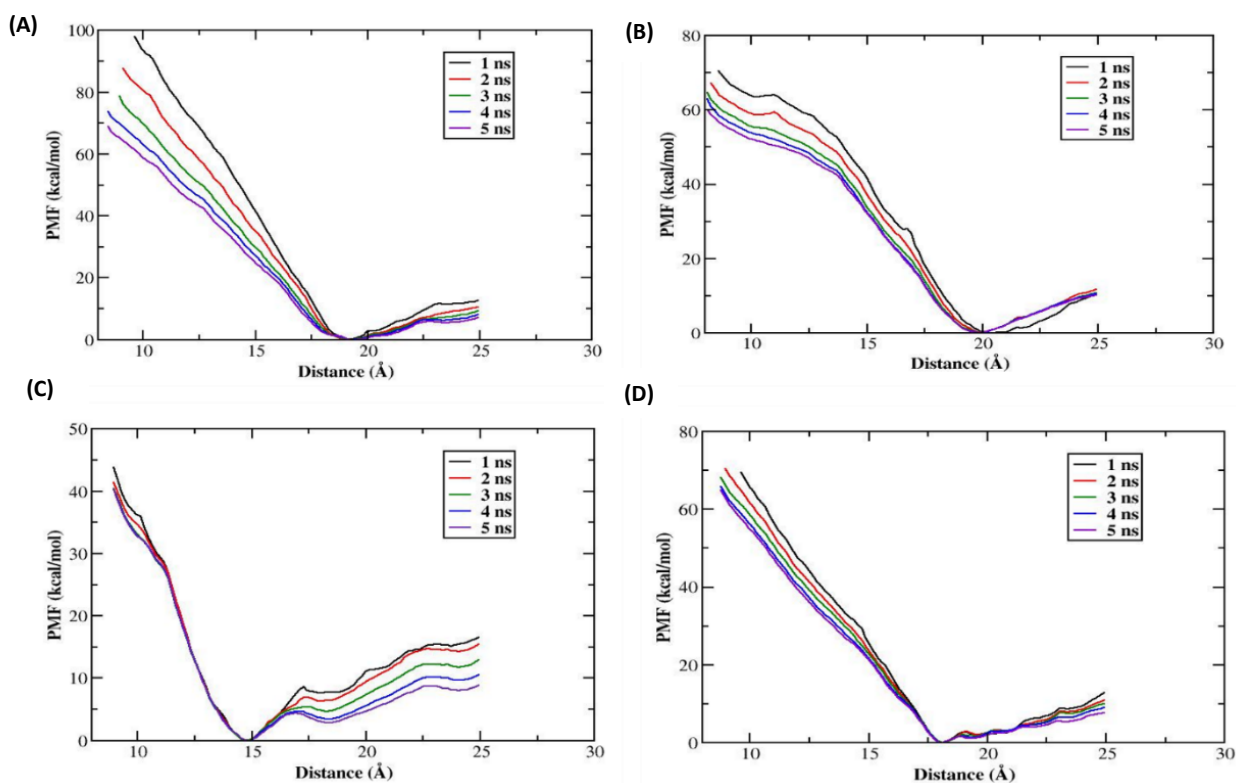
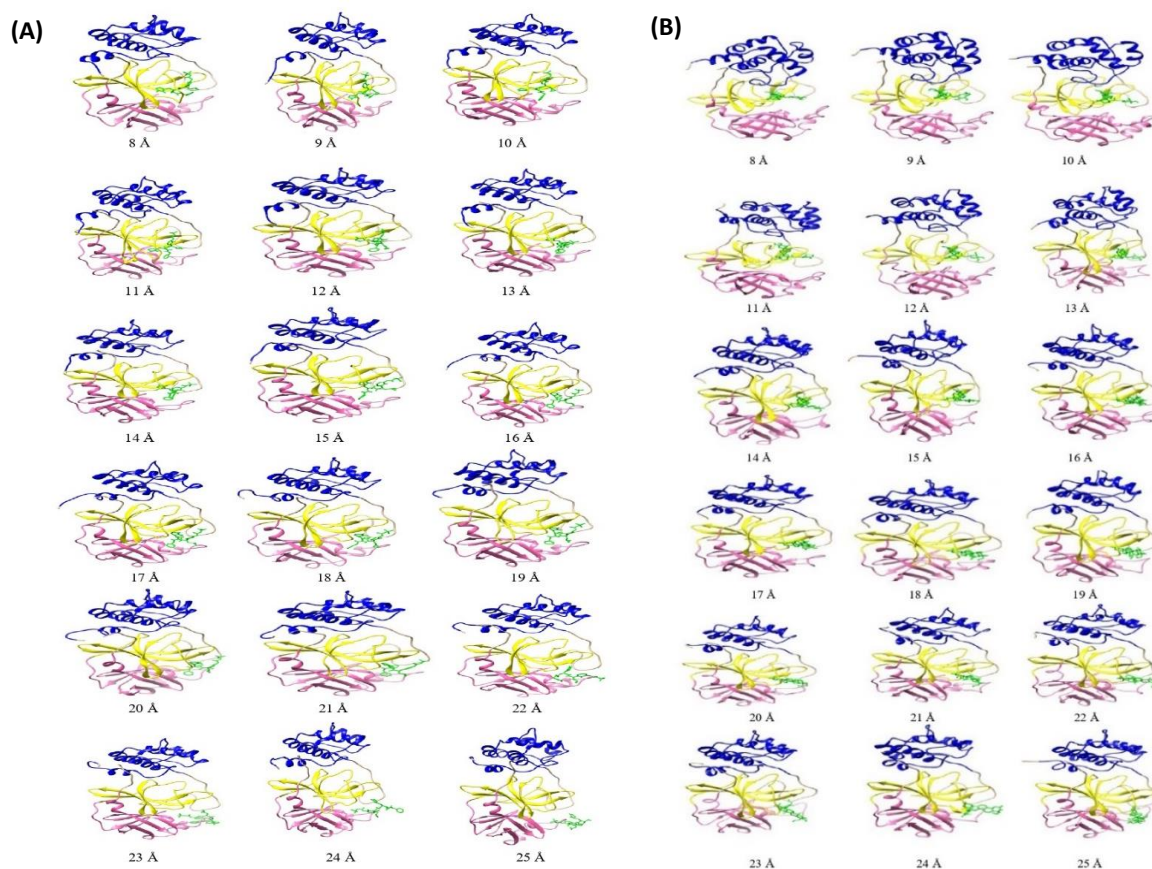


Figure 5.7. Convergence of the PMFs calculated by umbrella sampling for (A) SARS-CoV-2-Alpha-ketoamide (B) SARS-CoV-2-Arjunglucoside-I (C) SARS-CoV-2-Carnosol (D) SARS-CoV-2-Rosmanol complex where 5 ns US simulation were performed.

We observed use of distinct reaction coordinates (RCs), when small molecules dissociate from the AKA binding pocket of SARS-CoV-2 Mpro, as stated according to a comparative study of PMF curves. When ligands (small molecule inhibitors) moved out of the AKA binding pocket of SARS-CoV-2 Mpro, different phases vertical elevation of the PMF (**Figure 5.6**) were observed. The small molecules were seen to move out of the AKA binding pocket when the biased potential rises. In the case of the Arjunglucoside-I small molecule inhibitor (**Figure 5.6**), when the ligand moves out of the binding pocket of SARS-CoV-2 Mpro, the PMF of RCs is upgraded, and at 20 Å of RC, the ligand completely dissociates with a potential energy value of 12 kcal/mol. Similarly, as the PMF curve rises, the other small molecule inhibitors are seen gradually moving out of the binding pocket of SARS-CoV-2 Mpro (**Figure 5.6**). We detected an energy barrier when the AKA small molecule was unbound from the binding pocket of SARS-CoV-2 Mpro and at 22.0 Å of RC, with a potential energy value of 8 kcal/mol, AKA dissociates from its binding site far more easily than other small molecule inhibitors. The snapshots of all the complex systems taken at various windows of separation distances during the simulation were shown in **Figure 5.8**.



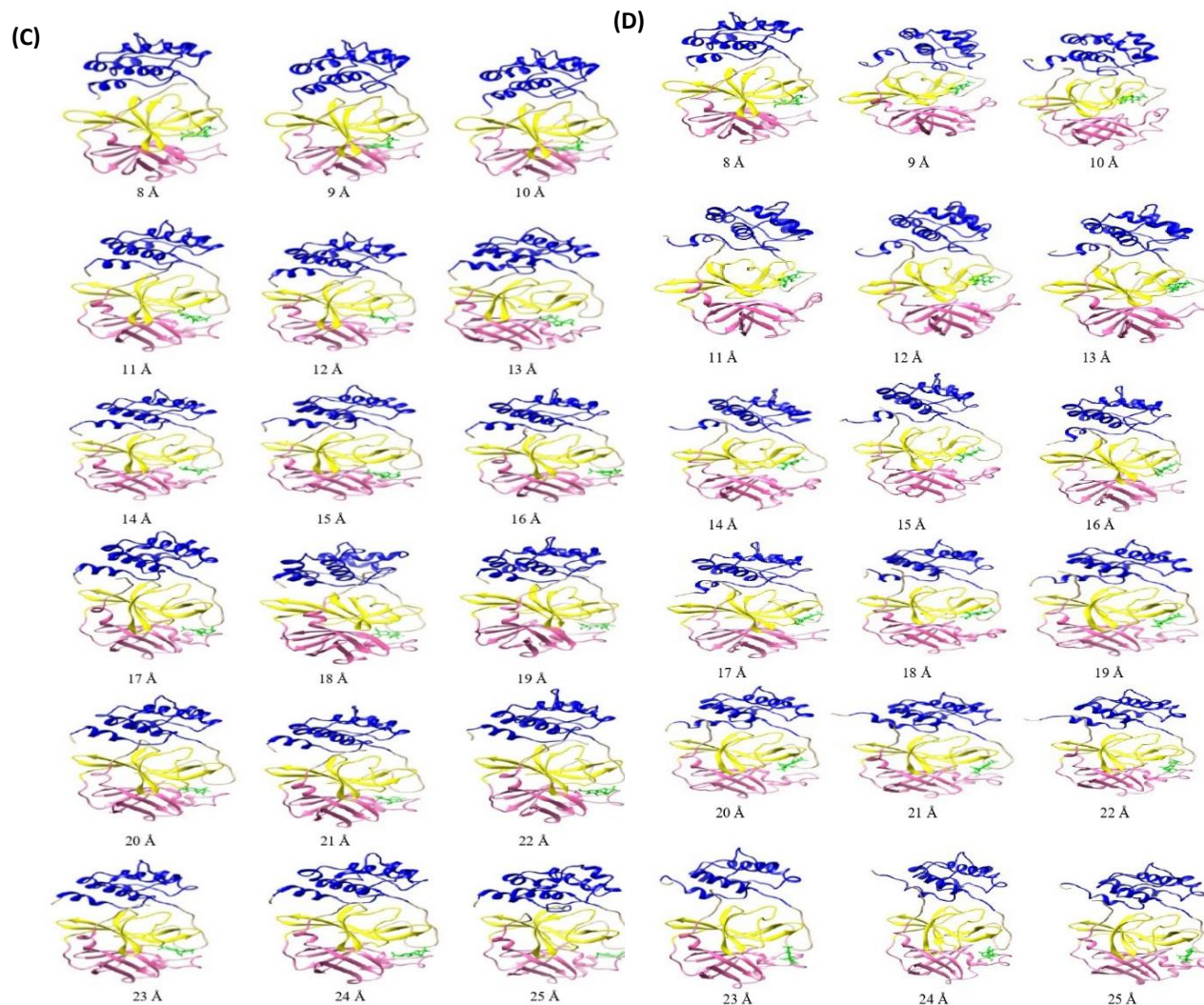


Figure 5.8. Snapshots of SARS-CoV-2 (A)Mpro-Alpha-ketoamide complex structures, (B) Mpro-Arjunglucoside-I complex, (C) Mpro-Carnosol complex structures and (D) Mpro-Rosmanol complex structures at discrete distance of separation (in Å) between their centre of mass.

The PMF profiles of all small molecule inhibitors and AKA with SARS-CoV-2 Mpro were compared. According to PMF plots, AKA has the lowest dissociation energy barrier of all the small molecules investigated here, and is thus expected to be easily released from the binding site of SARS-CoV-2 Mpro. The order of dissociation of small molecule inhibitors from the AKA binding site of SARS-CoV-2 Mpro was determined by PMF plots to be AKA < Rosmanol < Carnosol < Arjunglucoside-I.

From **Figure 5.6**, we see that the four small molecule- SARS-CoV-2 Mpro complexes show the minimum PMF values at different distances of separation and also exhibit different dissociation energy values in kcal/mol. The results have been summarized in **Table 5.2**.

Table 5.2. *Details of Umbrella Sampling Simulation*

Sl. no.	Name of the complex	Equilibrium distance (Å) at minimum PMF value	Dissociation energy (kcal/mol)	Distance samples (Å)	Duration (ns) for umbrella sampling, each window side being 5ns.
1	AKA- SARS-CoV-2 Mpro	19.5	9	8-25 Å	90 ns
2	ARJ- SARS-CoV-2 Mpro	20	11	8-25 Å	90 ns
3	CAN- SARS-CoV-2 Mpro	15	10	8-25 Å	90 ns
4	ROS- SARS-CoV-2 Mpro	17.5	9.5	8-25 Å	90 ns

When the distance between the small molecule inhibitors and the SARS-CoV-2 Mpro crosses 22 Å, we noticed that there are no more interactions between them. The PMF was observed to increase when the inter-molecular distance between SARS-CoV-2 Mpro and the small molecules was lowered below the optimum equilibrium distance (15 Å in the case of Carnosol, 18 Å in the case of Rosmanol, 19 Å in the case of Arjunglucoside-I and Alpha-ketoamide).

5.4.2. Salient structural features of the minimum PMF structure of the small molecule inhibitors-SARS-CoV-2 Mpro complex.

5.4.2.1. Molecular dynamics analysis.

Because it works with atomic-level interactions, MD is a useful computational tool for deciphering the physical foundation of biological macromolecule structure and function. From their corresponding 50 ns MD simulation trajectories, changes in the structure and stability of small molecule inhibitors-SARS-CoV-2 Mpro complexes were investigated. The trajectories obtained from 50 ns simulation for SARS-CoV-2 Mpro complexed with AKA (positive control), Arjunglucoside-I, Carnosol and Rosmanol were analyzed using the CPPTRAJ module of Amber program. The 3-D structure of the four complexes isolated at their minimum PMF value were used as starting structure for the corresponding simulation.

5.4.3. *Stability Profile Analysis of the SARs-CoV-2 Mpro protein-ligand complexes.*

The dynamic stability and structural behaviour of the SARS-CoV-2 Mpro-small molecule inhibitor complexes were investigated using MD simulations. The MD simulation data trajectory files were obtained over a 50-ns simulation time period.

5.4.3.1. **Root Mean Square Deviation (RMSD) analysis**

The atom-positional root mean-square deviation (RMSD) obtained from roto-translational least-squares fitting is likely the most commonly utilised measure for structural comparison and stability. The degree of structural variability in a particular ensemble is captured by RMSD values, which can be related to the intrinsic flexibility of a specific structure or the uncertainty of the structural refinements. The arithmetic mean is frequently used to summarise the parameters of this distribution, which is typically determined for backbone atoms. RMSD from the starting structure for the C- α backbone atoms from all the residues of Mpro complexed with AKA (positive control), Arjunglucoside-I, Carnosol and Rosmanol were calculated (**Figure 5.9**) from the 50 ns MD simulations. The simulation findings showed that when the Mpro was complexed with the small molecule inhibitors, the final RMSD variation from the initial model of C- and backbone atoms showed stable conformation, which was maintained throughout the simulation time of 50 ns. RMSD plots of Mpro complexed with the four ligands were similar, ranging between 0.7 Å and 1.7 Å. The amplitude of the fluctuation and the modest change in the average RMSD value of the C-backbone atoms, clearly shows that the four SARS-CoV-2 Mpro protein-ligand complex structures have a stable dynamic behaviour. In the four complexes, we have also calculated the RMSD of the four small molecule inhibitors (**Figure 5.10**) to check whether they are stable in the active site of SARS-CoV-2 and also to identify their possible binding modes. From the RMSD analysis of ligands, we found that among the four ligands, AKA showed larger fluctuations in the RMSD values. So, the small molecule inhibitors that have been identified from Indian spices are stable in the active site in comparison with the positive control.

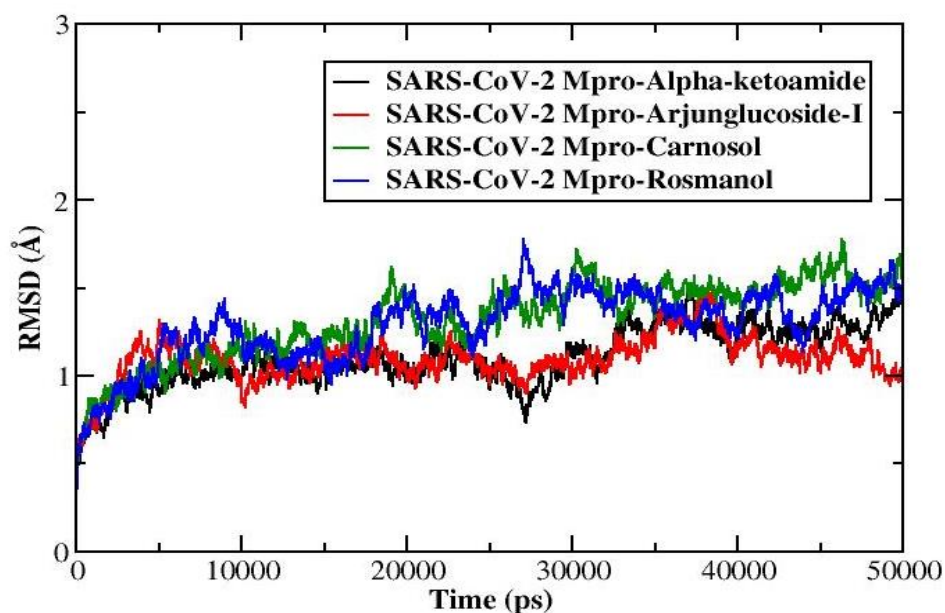


Figure 5.9. Root Mean Square Deviation (RMSD) analysis of the SARS-CoV-2 Mpro-small molecule inhibitor complexes as a function of simulation time in picoseconds (ps).

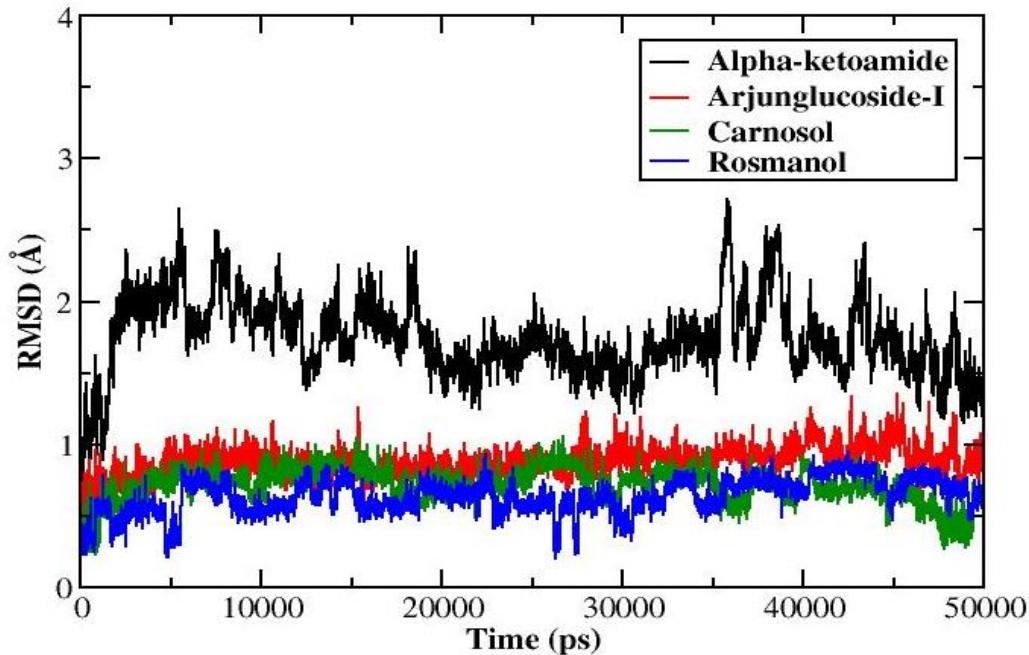


Figure 5.10. Root Mean Square Deviation (RMSD) analysis of the small molecule inhibitors in the complexes as a function of simulation time in picoseconds (ps).

5.4.3.2. Root Mean Square Fluctuation (RMSF) analysis

Residues RMSF analysis was used to determine the residues responsible for complex structural fluctuations in the four SARS-CoV-2 Mpro complexes (**Figure 5.11**). The average position of fluctuations of all the C α -atoms in the amino acid residues of the complex is depicted by RMSF analysis. In all the four SARS-CoV-2 Mpro-ligand complexes, greater fluctuations were observed at the residues near the binding site of the ligand.

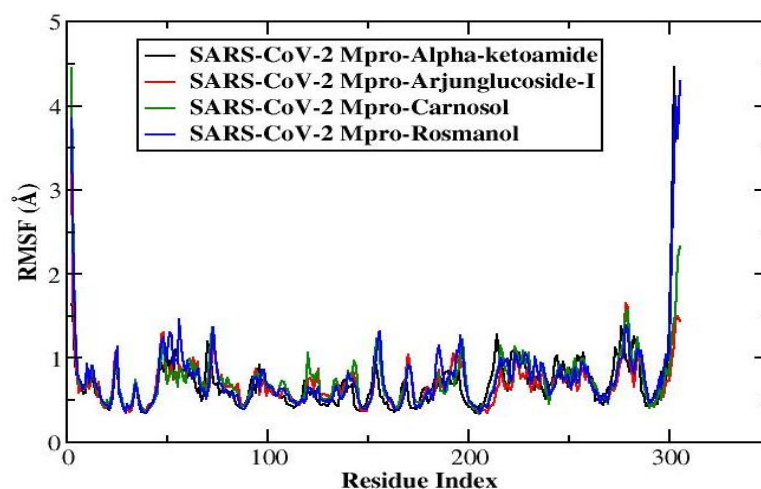


Figure 5.11. Root Mean Square Fluctuation (RMSF) Analysis of the SARS-CoV-2 Mpro-small molecule inhibitor complexes as a function of Residue index.

5.4.3.3. Radius of gyration (Rg) analysis.

The mass-weighted root-mean-square distance of atoms from their centre of mass is known as the radius of gyration (Rg). **Figure 5.12** depicts the information about the compactness, shape, and folding of the four complex structures at various point scales throughout the 50 ns of MD simulation trajectory. Throughout the 50 ns simulation time, all four complexes showed a similar pattern in terms of Rg value. It denotes the four complexes' long-term stability and compactness.

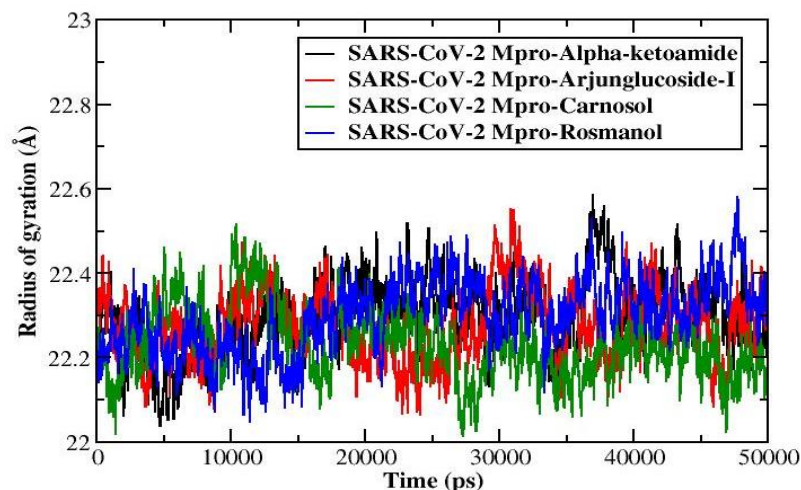


Figure 5.12. Radius of gyration analysis (R_g) of the SARS-CoV-2 Mpro-small molecule inhibitor complexes as a function of simulation time in picoseconds (ps).

5.4.3.4. Protein-ligand contact profiles.

From the MD simulation trajectories, the protein-ligand interaction patterns for all ligands with SARS-CoV-2 Mpro were obtained from the PDBsum server as shown in **Table 5.3-5.6** as well as from the LigPlot tool as shown in **Figure 5.13**. During the 50 ns simulation of the SARS-CoV-2 Mpro alpha-ketoamide complex, we found the residues GLU165, LEU166, PRO167, GLN188, ASN141, SER143, HIE162, HIE163, MET48, THR26 of SARS-CoV-2 Mpro have been involved in interaction with the ligand via hydrogen bonding, hydrophobic, ionic, and water bridge interactions. In other small molecule inhibitors-SARS-CoV-2 Mpro complexes, we see residues near the active site of Mpro were involved in interaction with the ligands through hydrogen bonding, hydrophobic, ionic and water bridges interactions during the 50 ns of simulation.

Table 5.3. List of atom-atom interactions(non-bonded) across protein-ligand interface in SARS-CoV2 Mpro- AKA complex from PDBsum server

SARS-CoV-2 Mpro					non-bonded	Alpha-ketoamide (AKA)				
Sl.no	Atom no.	Atom name	Res name	Res no.		Atom no.	Atom name	Res name	Res no.	Distance
1	2609	CD	GLU	165	----	1	O26	AKA	1	3.61
2	2611	OE2	GLU	165	----	1	O26	AKA	1	3.21

3	2631	C	LEU	166	----	5	C31	AKA	1	3.73
4	2633	N	PRO	167	----	5	C31	AKA	1	3.76
5	2945	NE2	GLN	188	----	11	O22	AKA	1	3.11
6	2945	NE2	GLN	188	----	16	C20	AKA	1	3.79
7	2266	CG	ASN	141	----	22	O37	AKA	1	3.65
8	2267	OD1	ASN	141	----	22	O37	AKA	1	3.15
9	2945	NE2	GLN	188	----	23	N38	AKA	1	3.74
10	2603	CB	GLU	165	----	27	C47	AKA	1	3.78
11	2603	CB	GLU	165	----	29	N49	AKA	1	3.43
12	2609	CD	GLU	165	----	29	N49	AKA	1	3.78
13	2610	OE1	GLU	165	----	29	N49	AKA	1	3.37
14	2610	OE1	GLU	165	----	30	C51	AKA	1	3.77
15	2287	OG	SER	143	----	31	C54	AKA	1	3.58
16	2557	CE1	HIE	162	----	31	C54	AKA	1	3.64
17	2559	NE2	HIE	162	----	31	C54	AKA	1	3.58
18	2581	O	HIE	163	----	32	C57	AKA	1	3.85
19	2945	NE2	GLN	188	----	33	O40	AKA	1	3.77
20	787	SD	MET	48	----	37	C13	AKA	1	3.59
21	788	CE	MET	48	----	38	C14	AKA	1	3.84
22	788	CE	MET	48	----	39	C28	AKA	1	3.52
23	439	CG2	THR	26	----	40	C26	AKA	1	3.79
24	2267	OD1	ASN	141	----	42	C23	AKA	1	3.24
25	2273	N	GLY	142	----	42	C23	AKA	1	3.87
26	2267	OD1	ASN	141	----	43	C15	AKA	1	3.6

Table 5.4A. List of atom-atom interactions (Hydrogen bonds) across protein-protein interface in SARS-Cov2- ARJ complex from PDBsum server.

SARS-CoV-2 Mpro					Hydrogen bonds	Arjunglucoside (ARJ)				
Sl.no	Atom	Atom	Res	Res		Atom	Atom	Res	Res	
	no.	name	name	no.		no.	name	name	no.	Distance
1	795	OG	SER	47	<--	9	O8	ARJG	1	3.24
2	722	NE2	HIE	42	-->	11	O10	ARJG	1	2.98
3	2629	O	HIE	165	<--	11	O10	ARJG	1	3.16

Table 5.4B. List of atom-atom interactions (non-bonded) across protein-protein interface in SARS-Cov2- ARJ complex from PDBsum server.

SARS-CoV-2 Mpro					non- bonded	Arjunglucoside (ARJ)				
Sl.no.	Atom	Atom	Res	Res		Atom	Atom	Res	Res	
	no.	name	name	no.		no.	name	name	no.	Distance
1	2272	CB	PHE	141	---	3	O2	ARJG	1	3.13

2	2275	CG	PHE	141	---	3	O2	ARJG	1	3.31
3	2284	CD2	PHE	141	---	3	O2	ARJG	1	3.8
4	2332	CB	SER	145	---	3	O2	ARJG	1	3.54
5	2632	CA	MET	166	---	6	O5	ARJG	1	3.84
6	2645	C	MET	166	---	6	O5	ARJG	1	3.59
7	2647	N	GLU	167	---	6	O5	ARJG	1	3.08
8	2649	CA	GLU	167	---	6	O5	ARJG	1	3.88
9	2651	CB	GLU	167	---	6	O5	ARJG	1	3.46
10	2629	O	HIE	165	---	7	O6	ARJG	1	3.42
11	2632	CA	MET	166	---	7	O6	ARJG	1	3.69
12	792	CB	SER	47	---	9	O8	ARJG	1	3.76
13	795	OG	SER	47	---	9	O8	ARJG	1	3.24
14	836	SD	MET	50	---	9	O8	ARJG	1	3.59
15	830	CB	MET	50	---	10	O9	ARJG	1	3.69
16	836	SD	MET	50	---	10	O9	ARJG	1	3.59
17	837	CE	MET	50	---	10	O9	ARJG	1	3.54
18	2959	CA	ARG	189	---	10	O9	ARJG	1	3.62
19	2979	C	ARG	189	---	10	O9	ARJG	1	3.6
20	2981	N	GLN	190	---	10	O9	ARJG	1	3.55
21	720	CE1	HIE	42	---	11	O10	ARJG	1	3.46
22	722	NE2	HIE	42	---	11	O10	ARJG	1	2.98
23	2629	O	HIE	165	---	11	O10	ARJG	1	3.16
24	2634	CB	MET	166	---	11	O10	ARJG	1	3.58
25	2947	CA	ASP	188	---	11	O10	ARJG	1	3.8
26	2955	C	ASP	188	---	11	O10	ARJG	1	3.43
27	2956	O	ASP	188	---	11	O10	ARJG	1	3.45
28	2659	OE2	GLU	167	---	22	C10	ARJG	1	3.45
29	2659	OE2	GLU	167	---	29	C17	ARJG	1	3.58
30	2658	OE1	GLU	167	---	31	C19	ARJG	1	3.68
31	2305	C	LEU	142	---	32	C20	ARJG	1	3.57
32	2306	O	LEU	142	---	32	C20	ARJG	1	3.35
33	2307	N	ASN	143	---	32	C20	ARJG	1	3.73
34	2309	CA	ASN	143	---	32	C20	ARJG	1	3.76
35	2628	C	HIE	165	---	34	C22	ARJG	1	3.58
36	2629	O	HIE	165	---	34	C22	ARJG	1	3.47
37	2630	N	MET	166	---	34	C22	ARJG	1	3.57
38	2632	CA	MET	166	---	34	C22	ARJG	1	3.8
39	2339	N	CYS	146	---	38	C26	ARJG	1	3.78
40	2341	CA	CYS	146	---	38	C26	ARJG	1	3.49
41	2343	CB	CYS	146	---	38	C26	ARJG	1	3.77
42	2346	SG	CYS	146	---	38	C26	ARJG	1	3.78
43	2612	O	HIE	164	---	38	C26	ARJG	1	3.85
44	2630	N	MET	166	---	40	C28	ARJG	1	3.71

45	2645	C	MET	166	---	40	C28	ARJG	1	3.9
46	2646	O	MET	166	---	40	C28	ARJG	1	3.38
47	2745	CD2	HIE	173	---	40	C28	ARJG	1	3.9
48	2337	C	SER	145	---	41	C29	ARJG	1	3.74
49	2338	O	SER	145	---	41	C29	ARJG	1	3.38
50	2634	CB	MET	166	---	47	C35	ARJG	1	3.73
51	2955	C	ASP	188	---	47	C35	ARJG	1	3.7
52	2957	N	ARG	189	---	47	C35	ARJG	1	3.73
53	2980	O	ARG	189	---	47	C35	ARJG	1	3.61

Table 5.5A. List of atom-atom interactions (Hydrogen bonds) across protein-protein interface in SARS-Cov2- CAN complex from PDBsum server.

SARS-CoV-2 Mpro					Hydrogen bonds	Carnosol (CAN)				
Sl.no	Atom	Atom	Res	Res		Atom	Atom	Res	Res	
	no.	name	name	no.		No.	name	name	no.	Distance
1	667	NE2	HIE	42		3	O3	CAN	1	3.27

Table 5.5B. List of atom-atom interactions (non-bonded) across protein-protein interface in SARS-Cov2- CAN complex from PDBsum server.

SARS-CoV-2 Mpro					non-bonded	Carnosol (CAN)				
Sl.no.	Atom	Atom	Res	Res		Atom	Atom	Res	Res	
	no.	name	name	no.		no.	name	name	no.	Distance
1	2593	N	GLU	167	---	1	O1	CAN	1	3.28
2	2607	O	GLU	167	---	1	O1	CAN	1	3.5
3	2597	CB	GLU	167	---	1	O1	CAN	1	3.83
4	667	NE2	HIE	42	---	3	O3	CAN	1	3.27
5	669	CD2	HIE	42	---	3	O3	CAN	1	3.76
6	2580	CB	MET	166	---	3	O3	CAN	1	3.8
7	2926	O	ARG	189	---	3	O3	CAN	1	3.78
8	663	CG	HIE	42	---	4	O4	CAN	1	3.72
9	664	ND1	HIE	42	---	4	O4	CAN	1	3.42
10	665	CE1	HIE	42	---	4	O4	CAN	1	2.39
11	667	NE2	HIE	42	---	4	O4	CAN	1	2.1
12	669	CD2	HIE	42	---	4	O4	CAN	1	3.09
13	2563	CB	HIE	165	---	4	O4	CAN	1	3.67
14	2574	C	HIE	165	---	4	O4	CAN	1	3.53
15	2575	O	HIE	165	---	4	O4	CAN	1	2.99
16	2578	CA	MET	166	---	5	C1	CAN	1	3.79
17	2591	C	MET	166	---	5	C1	CAN	1	3.88
18	2580	CB	MET	166	---	5	C1	CAN	1	3.15

19	2587	CE	MET	166	---	5	C1	CAN	1	3.2
20	2593	N	GLU	167	---	5	C1	CAN	1	3.4
21	2606	C	GLU	167	---	5	C1	CAN	1	3.59
22	2607	O	GLU	167	---	5	C1	CAN	1	2.79
23	2580	CB	MET	166	---	6	C2	CAN	1	3.51
24	2587	CE	MET	166	---	7	C3	CAN	1	3.24
25	2606	C	GLU	167	---	7	C3	CAN	1	3.88
26	2607	O	GLU	167	---	7	C3	CAN	1	2.85
27	2972	CB	GLN	193	---	7	C3	CAN	1	3.53
28	2980	NE2	GLN	193	---	7	C3	CAN	1	3.7
29	2578	CA	MET	166	---	8	C4	CAN	1	3.24
30	2591	C	MET	166	---	8	C4	CAN	1	2.85
31	2592	O	MET	166	---	8	C4	CAN	1	3.81
32	2580	CB	MET	166	---	8	C4	CAN	1	3.25
33	2587	CE	MET	166	---	8	C4	CAN	1	3.85
34	2593	N	GLU	167	---	8	C4	CAN	1	2
35	2595	CA	GLU	167	---	8	C4	CAN	1	2.55
36	2606	C	GLU	167	---	8	C4	CAN	1	2.36
37	2607	O	GLU	167	---	8	C4	CAN	1	1.89
38	2597	CB	GLU	167	---	8	C4	CAN	1	3.39
39	2608	N	LEU	168	---	8	C4	CAN	1	3.61
40	2926	O	ARG	189	---	9	C5	CAN	1	3.32
41	2929	CA	GLN	190	---	9	C5	CAN	1	3.7
42	2980	NE2	GLN	193	---	9	C5	CAN	1	3.81
43	2587	CE	MET	166	---	10	C6	CAN	1	3.27
44	2957	O	THR	191	---	10	C6	CAN	1	3.39
45	2972	CB	GLN	193	---	10	C6	CAN	1	2.85
46	2975	CG	GLN	193	---	10	C6	CAN	1	2.87
47	2978	CD	GLN	193	---	10	C6	CAN	1	2.81
48	2980	NE2	GLN	193	---	10	C6	CAN	1	2.28
49	2578	CA	MET	166	---	11	C7	CAN	1	2.85
50	2591	C	MET	166	---	11	C7	CAN	1	2.79
51	2580	CB	MET	166	---	11	C7	CAN	1	3.37
52	2593	N	GLU	167	---	11	C7	CAN	1	1.94
53	2595	CA	GLU	167	---	11	C7	CAN	1	2.92
54	2606	C	GLU	167	---	11	C7	CAN	1	3.38
55	2607	O	GLU	167	---	11	C7	CAN	1	3.11
56	2597	CB	GLU	167	---	11	C7	CAN	1	3.19
57	2578	CA	MET	166	---	12	C8	CAN	1	2.93
58	2591	C	MET	166	---	12	C8	CAN	1	3.85
59	2580	CB	MET	166	---	12	C8	CAN	1	2.52
60	2593	N	GLU	167	---	12	C8	CAN	1	3.77
61	2926	O	ARG	189	---	13	C9	CAN	1	2.77

62	2957	O	THR	191	---	13	C9	CAN	1	3.68
63	2975	CG	GLN	193	---	13	C9	CAN	1	3.76
64	2978	CD	GLN	193	---	13	C9	CAN	1	3.32
65	2980	NE2	GLN	193	---	13	C9	CAN	1	2.26
66	2574	C	HIE	165	---	14	C10	CAN	1	3.78
67	2575	O	HIE	165	---	14	C10	CAN	1	3.45
68	2576	N	MET	166	---	14	C10	CAN	1	3.33
69	2578	CA	MET	166	---	14	C10	CAN	1	2.05
70	2591	C	MET	166	---	14	C10	CAN	1	2.82
71	2580	CB	MET	166	---	14	C10	CAN	1	2.44
72	2593	N	GLU	167	---	14	C10	CAN	1	2.68
73	2607	O	GLU	167	---	16	C12	CAN	1	2.89
74	2587	CE	MET	166	---	17	C13	CAN	1	2.6
75	2606	C	GLU	167	---	17	C13	CAN	1	3.37
76	2607	O	GLU	167	---	17	C13	CAN	1	2.64
77	2608	N	LEU	168	---	17	C13	CAN	1	3.86
78	2610	CA	LEU	168	---	17	C13	CAN	1	3.72
79	2615	CG	LEU	168	---	17	C13	CAN	1	3.11
80	2621	CD2	LEU	168	---	17	C13	CAN	1	2.55
81	2972	CB	GLN	193	---	17	C13	CAN	1	3.15
82	667	NE2	HIE	42	---	18	C14	CAN	1	3.8
83	2575	O	HIE	165	---	18	C14	CAN	1	3.7
84	2578	CA	MET	166	---	18	C14	CAN	1	3.51
85	2580	CB	MET	166	---	18	C14	CAN	1	2.92
86	2574	C	HIE	165	---	19	C15	CAN	1	2.67
87	2575	O	HIE	165	---	19	C15	CAN	1	2.16
88	2576	N	MET	166	---	19	C15	CAN	1	2.56
89	2578	CA	MET	166	---	19	C15	CAN	1	1.89
90	2591	C	MET	166	---	19	C15	CAN	1	2.96
91	2580	CB	MET	166	---	19	C15	CAN	1	2.78
92	2593	N	GLU	167	---	19	C15	CAN	1	3.23
93	2561	CA	HIE	165	---	20	C16	CAN	1	3.39
94	2574	C	HIE	165	---	20	C16	CAN	1	2.17
95	2575	O	HIE	165	---	20	C16	CAN	1	1.3
96	2576	N	MET	166	---	20	C16	CAN	1	2.74
97	2578	CA	MET	166	---	20	C16	CAN	1	2.67
98	2580	CB	MET	166	---	20	C16	CAN	1	3.14
99	665	CE1	HIE	42	---	21	C17	CAN	1	3.76
100	667	NE2	HIE	42	---	21	C17	CAN	1	3.32
101	2574	C	HIE	165	---	21	C17	CAN	1	3.13
102	2575	O	HIE	165	---	21	C17	CAN	1	2.51
103	2576	N	MET	166	---	21	C17	CAN	1	3.62
104	2578	CA	MET	166	---	21	C17	CAN	1	3.33

105	2580	CB	MET	166	---	21	C17	CAN	1	3.11
106	2287	CA	CYS	146	---	22	C18	CAN	1	3.73
107	2289	CB	CYS	146	---	22	C18	CAN	1	3.27
108	2292	SG	CYS	146	---	22	C18	CAN	1	2.86
109	2559	N	HIE	165	---	22	C18	CAN	1	3.73
110	2561	CA	HIE	165	---	22	C18	CAN	1	2.53
111	2563	CB	HIE	165	---	22	C18	CAN	1	3.5
112	2574	C	HIE	165	---	22	C18	CAN	1	1.69
113	2575	O	HIE	165	---	22	C18	CAN	1	0.55
114	2576	N	MET	166	---	22	C18	CAN	1	2.83
115	2578	CA	MET	166	---	22	C18	CAN	1	3.46
116	2287	CA	CYS	146	---	23	C19	CAN	1	3.8
117	2292	SG	CYS	146	---	23	C19	CAN	1	3.56
118	2550	ND1	HIE	164	---	23	C19	CAN	1	3.11
119	2551	CE1	HIE	164	---	23	C19	CAN	1	3.5
120	2557	C	HIE	164	---	23	C19	CAN	1	3.31
121	2558	O	HIE	164	---	23	C19	CAN	1	3.64
122	2559	N	HIE	165	---	23	C19	CAN	1	2.32
123	2561	CA	HIE	165	---	23	C19	CAN	1	1.44
124	2563	CB	HIE	165	---	23	C19	CAN	1	2.82
125	2574	C	HIE	165	---	23	C19	CAN	1	0.8
126	2575	O	HIE	165	---	23	C19	CAN	1	1.3
127	2576	N	MET	166	---	23	C19	CAN	1	1.93
128	2578	CA	MET	166	---	23	C19	CAN	1	3.14
129	2285	N	CYS	146	---	24	C20	CAN	1	3.46
130	2287	CA	CYS	146	---	24	C20	CAN	1	2.91
131	2289	CB	CYS	146	---	24	C20	CAN	1	2.31
132	2292	SG	CYS	146	---	24	C20	CAN	1	2.8
133	2561	CA	HIE	165	---	24	C20	CAN	1	3.74
134	2574	C	HIE	165	---	24	C20	CAN	1	2.96
135	2575	O	HIE	165	---	24	C20	CAN	1	1.92
136	2576	N	MET	166	---	24	C20	CAN	1	3.89

Table 5.6A. List of atom-atom interactions across protein-protein interface in SARS-Cov2- ROS complex from PDBsum server.

SARS-CoV-2 Mpro					Hydrogen bonds	Rosmanol (ROS)				
Sl.no	Atom no.	Atom name	Res name	Res no.		Atom no.	Atom name	Res name	Res no.	Distance
1	2234	O	PHE	141	<--	1	O1	ROS	1	3.30
2	2554	NE2	HIE	164	<--	3	O3	ROS	1	3.20
3	2561	NE2	HIE	178	<--	5	O5	ROS	1	3.28

Table 5.6B. List of atom-atom interactions (non-bonded) across protein-protein interface in SARS-Cov2- ROS complex from PDBsum server.

SARS-CoV-2 Mpro					non-bonded	Rosmanol (ROS)				
Sl.no	Atom	Atom	Res	Res		Atom	Atom	Res	Res	
	no.	name	name	no.		no.	name	name	no.	Distance
1	2234	O	PHE	141	---	1	O1	ROS	1	3.3
2	2598	CB	GLU	167	---	1	O1	ROS	1	3.81
3	2605	OE1	GLU	167	---	1	O1	ROS	1	3.9
4	2552	CE1	HIE	164	---	3	O3	ROS	1	3.82
5	2554	NE2	HIE	164	---	3	O3	ROS	1	3.2
6	2579	CA	MET	166	---	3	O3	ROS	1	3.38
7	2592	C	MET	166	---	3	O3	ROS	1	3.15
8	2593	O	MET	166	---	3	O3	ROS	1	3.75
9	2594	N	GLU	167	---	3	O3	ROS	1	3.14
10	2598	CB	GLU	167	---	3	O3	ROS	1	3.55
11	2579	CA	MET	166	---	4	O4	ROS	1	3.88
12	2581	CB	MET	166	---	4	O4	ROS	1	3.52
13	2594	N	GLU	167	---	4	O4	ROS	1	3.47
14	2944	O	GLN	190	---	4	O4	ROS	1	3.51
15	2608	O	GLU	167	---	5	O5	ROS	1	3.28
16	2944	O	GLN	190	---	5	O5	ROS	1	3.75
17	2234	O	PHE	141	---	9	C4	ROS	1	3.46
18	2594	N	GLU	167	---	12	C7	ROS	1	3.85
19	2598	CB	GLU	167	---	12	C7	ROS	1	3.68
20	2604	CD	GLU	167	---	14	C9	ROS	1	3.83
21	2605	OE1	GLU	167	---	14	C9	ROS	1	3.88
22	2606	OE2	GLU	167	---	14	C9	ROS	1	3.74
23	2594	N	GLU	167	---	15	C10	ROS	1	3.69
24	2598	CB	GLU	167	---	15	C10	ROS	1	3.56
25	2598	CB	GLU	167	---	16	C11	ROS	1	3.7
26	2234	O	PHE	141	---	17	C12	ROS	1	3.74
27	2252	C	LEU	142	---	17	C12	ROS	1	3.89
28	2253	O	LEU	142	---	17	C12	ROS	1	3.12
29	2282	OG	SER	145	---	17	C12	ROS	1	3.21
30	2594	N	GLU	167	---	19	C14	ROS	1	3.58
31	2608	O	GLU	167	---	19	C14	ROS	1	3.84
32	2598	CB	GLU	167	---	20	C15	ROS	1	3.85
33	2604	CD	GLU	167	---	20	C15	ROS	1	3.88
34	2606	OE2	GLU	167	---	20	C15	ROS	1	3.41
35	2608	O	GLU	167	---	22	C17	ROS	1	3.49
36	2608	O	GLU	167	---	24	C19	ROS	1	3.6

37	2626	C	LEU	168	---	24	C19	ROS	1	3.77
38	2963	CB	ALA	192	---	25	C20	ROS	1	3.78

The protein-ligand interaction patterns for all ligands with SARS-CoV-2 Mpro obtained from the LigPlot tool are depicted in **Figure 5.13**.

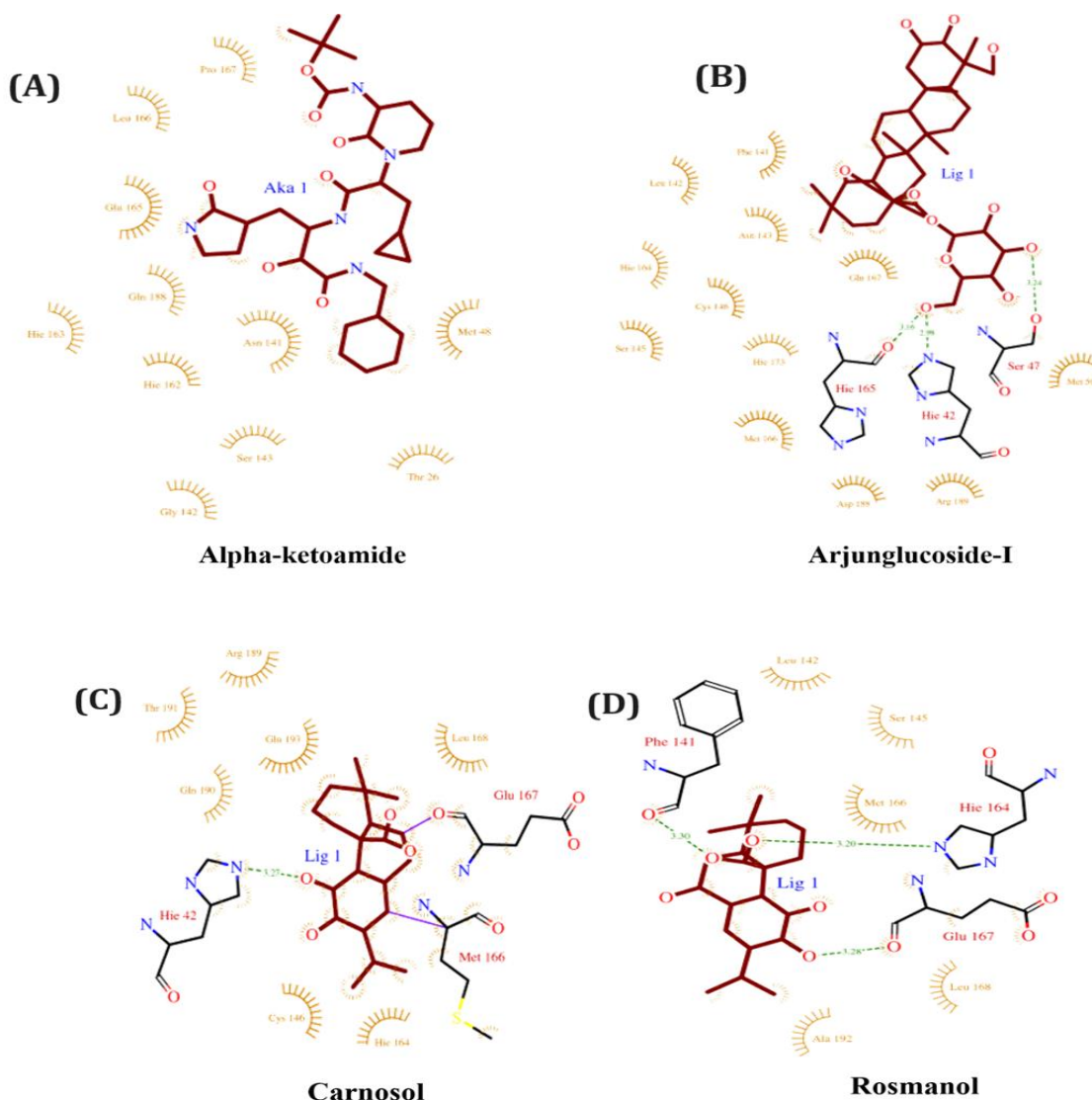


Figure 5.13. Amino acid residual interactions of the protein-ligand interface in (A) SARS-CoV-2-Alpha-ketoamide (B) SARS-CoV-2-Arjunglucoside-I (C) SARS-CoV-2-Carnosol (D) SARS-CoV-2-Rosmanol complexes. The hydrogen bond interactions are represented by dashed lines. The amino acid residues involved in the hydrophobic interactions are shown as starbursts.

In addition, we have also determined the total number of inter-molecular hydrogen bonds at different points throughout the 50 ns simulation time in the four complexes as shown in **Figure 5.14**. From the

plots we can see for the four complexes, the number of inter-molecular hydrogen bonds follows the order SARS-CoV-2 Mpro-Arjunglucoside > SARS-CoV-2 Mpro-Carnosol > SARS-CoV-2 Mpro- Alpha-ketoamide > SARS-CoV-2 Mpro-Rosmanol. These observations suggested the ligands from Indian spices as strong inhibitor against SARS-CoV-2 Mpro.

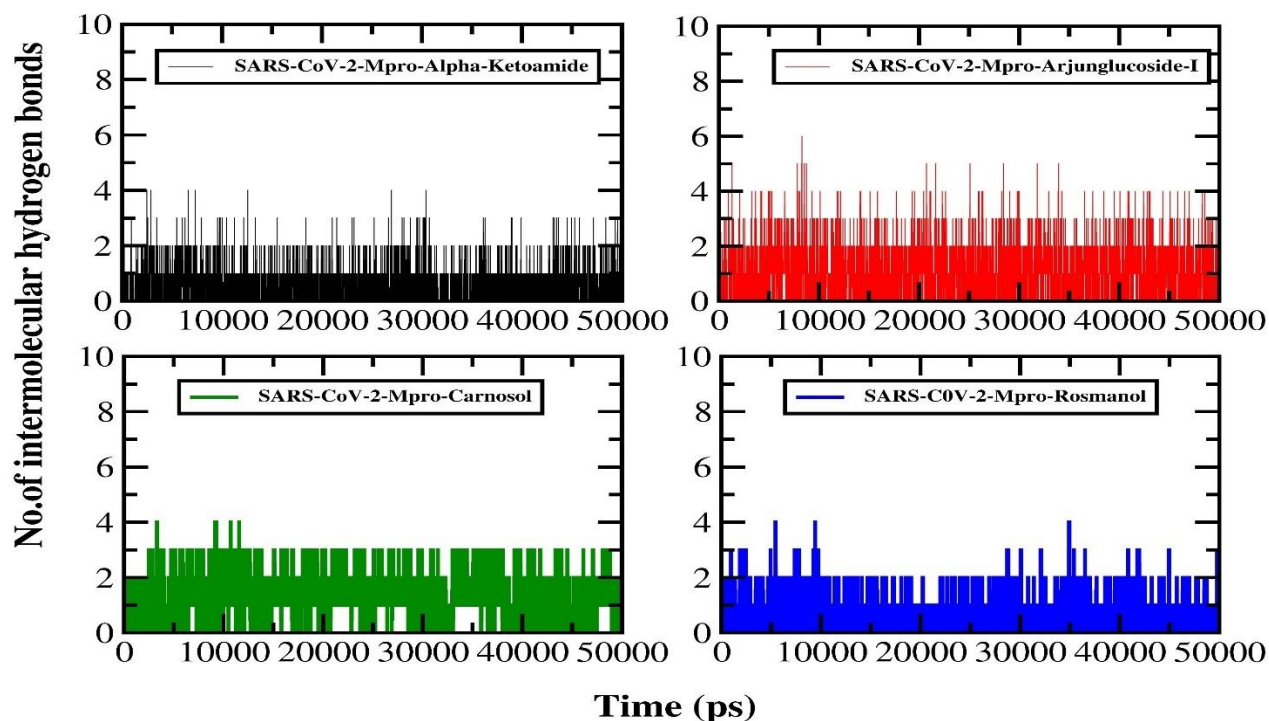


Figure 5.14. Number of inter-molecular hydrogen bonds between SARS-CoV-2 Mpro and the small molecule inhibitors as a function of simulation time in picoseconds (ps).

5.4.3.5. Binding free energy (BFE) and per residue energy decomposition (PRED) analysis.

The molecular mechanic energies were integrated using the MM-PBSA/GBSA method to further study the free energy of the binding of small molecules with the SARS-CoV-2 Mpro. Because MM-PBSA/GBSA approach uses a continuum solvent technique to determine the binding free energies of a complex system, the binding energy values here represent the relative binding free energy, not the absolute or total binding free energy. The main goal of these methods is to determine the difference in free energy between the bound and unbound states of protein-ligand complexes. For all of the protein-ligand complexes, the MM-PBSA/GBSA approach was used to calculate all of the thermochemical characteristics by using the AMBER suite for each coordinate at every 10 ps sampling frequency throughout the MD trajectory. The most stable complexes were considered to be the those with the lowest

binding energy. The binding free energy analysis for SARS-CoV-2 Mpro- small molecule inhibitor complexes were tabulated in **Table 5.7** to **Table 5.14**. The total free energies (ΔG_{bind}) obtained from MM-GBSA and MM-PBSA for the protein-ligand complexes show comparable values (-13.14 kcal/mol from MM-GBSA and -5.31 kcal/mol from MM-PBSA for the SARS-CoV-2 Mpro-Alpha-ketoamide complex, -19.74 kcal/mol from MM-GBSA and -9.13 kcal/mol from MM-PBSA for the SARS-CoV-2 Mpro-Arjunglucoside-I complex, -16.81 kcal/mol from MM-GBSA and -9.98 kcal/mol from MM-PBSA for the SARS-CoV-2 Mpro-Carnosol complex, -14.05 kcal/mol from MM-GBSA and -5.87 kcal/mol from MM-PBSA for the SARS-CoV-2 Mpro-Rosmanol complex). ΔG_{bind} for the SARS-CoV-2 Mpro showed the least value for the SARS-CoV-2 Mpro and Arjunglucoside-I complex followed by SARS-CoV-2 Mpro-Carnosol complex, SARS-CoV-2 Mpro-Rosmanol complex and SARS-CoV-2 Mpro-Alpha-ketoamide complex. These observations suggest the small molecule obtained from Indian spices as potential inhibitors of SARS-CoV-2 Mpro.

Table 5.7. The various components of the Binding Free Energy (kcal/mol) evaluated by Molecular Mechanics-Generalized Borne Surface Area (MM-GBSA) method between SARS-CoV-2 main protease (Mpro) – alpha ketoamide (AKA) complex.

	Average (Mpro-AKA) (kcal/mol)	Average (Mpro) (kcal/mol)	Average (AKA) (kcal/mol)	▲ (kcal/mol)
VDW	-2403.67	-2363.27	-1.83	-38.57
ELE	-21647.22	-21576.06	-58.59	-12.56
GB	-2610.86	-2601.34	-19.29	9.77
GBSUR	103.86	105.04	3.36	-4.54
GAS	-24050.90	-23939.33	-60.43	-51.13
GBSOL	-2506.99	-2516.29	-15.92	25.22
GBTOT	-26557.89	-26445.63	-76.35	-35.90
TSTRA	17.01	16.99	13.42	-13.40
TSROT	17.72	17.70	11.43	-11.41
TSVIB	3314.02	3258.52	53.45	2.05
TSTOT	3348.75	3293.22	78.30	-22.76
ΔG_{bind}	-13.14			

Electrostatic energy (ELE); van der Waals contribution (VDW); total gas phase energy (GAS); nonpolar contribution to the solvation free energy (GBSUR); the electrostatic contribution to the solvation free energy (GB); sum of nonpolar and polar contributions to solvation (GBSOL); final estimated binding free energy (GBTOT); translational energy

(**TSTRA**); rotational energy (**TSROT**); vibrational energy (**TSVIB**), total entropic contribution (**TSTOT**); binding free energy (ΔG_{bind}).

Table 5.8. The various components of the Binding Free Energy (kcal/mol) evaluated by Molecular Mechanics- Poisson-Boltzmann Surface Area (MM-PBSA) method between SARS-CoV-2 main protease (Mpro) – alpha ketoamide (AKA) complex

	Average (Mpro-AKA) (kcal/mol)	Average (Mpro) (kcal/mol)	Average (AKA) (kcal/mol)	▲ (kcal/mol)
VDW	-2403.67	-2363.27	-1.83	-38.57
ELE	-21647.22	-21576.06	-58.59	-12.56
PB	-2650.11	-2664.57	-21.09	35.55
NPOLAR	2328.40	2376.58	37.43	-85.43
DISPER	-1307.40	-1314.42	-35.99	43.01
GAS	-24050.90	-23939.33	-60.43	-51.13
PBSOL	-1629.11	-1662.51	-19.65	53.06
PBTOL	-25680.01	-25570.76	-80.08	-28.07
TSTRA	17.01	16.99	13.42	-13.40
TSTRO	17.72	17.70	11.43	-11.41
TSVIB	3314.02	3258.52	53.45	2.05
TSTOL	3348.75	3293.22	78.30	-22.76
ΔG_{bind}	-5.31			

Electrostatic energy (**ELE**); van der Waals contribution (**VDW**); total gas phase energy (**GAS**); nonpolar contribution to the solvation free energy (**GBSUR**); the electrostatic contribution to the solvation free energy (**GB**); sum of nonpolar and polar contributions to solvation (**GBSOL**); final estimated binding free energy (**GBTOT**); translational energy (**TSTRA**); rotational energy (**TSROT**); vibrational energy (**TSVIB**), total entropic contribution (**TSTOT**); binding free energy (ΔG_{bind}).

Table 5.9. The various components of the Binding Free Energy (kcal/mol) evaluated by Molecular Mechanics-Generalized Borne Surface Area (MM-GBSA) method between SARS-CoV-2 main protease (Mpro)–arjunglucoside-I(ARJ) complex.

	Average (Mpro-ARJ) (kcal/mol)	Average (Mpro) (kcal/mol)	Average (ARJ) (kcal/mol)	▲ (kcal/mol)
VDW	-2354.72	-2318.97	-1.78	-33.96
ELE	-21639.86	-21531.04	-94.56	-14.25

GB	-2619.47	-2592.13	-23.86	-3.48
GBSUR	107.75	108.00	3.46	-3.71
GAS	-23994.59	-23850.02	-96.35	-48.21
GBSOL	-2511.71	-2514.12	-20.40	22.81
GBTOT	-26506.30	-26349.14	-116.75	-40.39
TSTRA	17.01	16.99	13.51	-13.50
TSROT	17.73	17.71	11.75	-11.73
TSVIB	3328.01	3272.04	51.38	4.58
TSTOT	3362.75	3306.75	76.65	-20.65
ΔG_{bind}	-19.74			

Table 5.10. The various components of the Binding Free Energy (kcal/mol) evaluated by Molecular Mechanics-Poisson-Boltzmann Surface Area (MM-PBSA) method between SARS-CoV-2 main protease (Mpro)–Arjunglucoside-I (ARJ) complex.

	Average (Mpro-ARJ) (kcal/mol)	Average (Mpro) (kcal/mol)	Average (ARJ) (kcal/mol)	Δ (kcal/mol)
VDW	-2354.72	-2318.97	-1.78	-33.96
ELE	-21639.86	-21531.04	-94.56	-14.25
PB	-2649.89	-2658.20	-26.25	34.56
NPOLAR	2356.32	2410.29	37.98	-91.95
DISPER	-1345.89	-1349.73	-36.98	40.82
GAS	-23994.59	-23850.02	-96.35	-48.21
PBSOL	-1639.46	-1667.64	-25.25	53.43
PBTOL	-25634.05	-25481.67	-121.60	-29.78
TSTRA	17.01	16.99	13.51	-13.50
TSTRO	17.73	17.71	11.75	-11.73
TSVIB	3328.01	3272.04	51.38	4.58
TSTOL	3362.75	3306.75	76.65	-20.65
ΔG_{bind}	-9.13			

Table 5.11. The various components of the Binding Free Energy (kcal/mol) evaluated by Molecular Mechanics-Generalized Borne Surface Area (MM-GBSA) method between SARS-CoV-2 main protease (Mpro) – Carsonol(CAN) complex.

	Average (Mpro-CAN) (kcal/mol)	Average (Mpro) (kcal/mol)	Average (CAN) (kcal/mol)	▲ (kcal/mol)
VDW	-2371.15	-2325.41	-1.60	-44.13
ELE	-21486.26	-21408.65	-59.01	-18.60
GB	-2790.09	-2803.01	-19.54	32.46
GBSUR	-110.37	-111.65	3.37	-4.65
GAS	-23857.42	-23734.06	-60.61	-62.47
GBSOL	-2679.72	-2691.36	-16.17	27.81
GBTOT	-26537.14	-26425.43	-76.78	-34.93
TSTRA	17.01	16.99	12.89	-12.88
TSROT	17.71	17.71	10.32	-10.32
TSVIB	3294.63	3268.39	21.15	5.08
TSTOT	3329.35	3303.11	44.37	-18.12
ΔG_{bind}	-16.81			

Table 5.12. The various components of the Binding Free Energy (kcal/mol) evaluated by Molecular Mechanics- Poisson-Boltzmann Surface Area (MM-PBSA) method between SARS-CoV-2 main protease (Mpro) – Carsonol (CAN complex).

	Average (Mpro-CAN) (kcal/mol)	Average (Mpro) (kcal/mol)	Average (CAN) (kcal/mol)	▲ (kcal/mol)
VDW	-2371.15	-2325.41	-1.60	-44.13
ELE	-21486.26	-21408.65	-59.01	-18.60
PB	-2838.37	-2849.99	-21.30	32.92
NPOLAR	2362.69	2393.40	37.32	-68.03
DISPER	-1351.53	-1365.30	-35.96	49.74
GAS	-23857.42	-23734.06	-60.61	-62.74

PBSOL	-1827.20	-1861.89	-19.95	54.63
PBTOL	-25684.63	-25575.96	-80.56	-28.10
TSTRA	17.01	16.99	12.89	-12.88
TSTRO	17.71	17.71	10.32	-10.32
TSVIB	3294.63	3268.39	21.15	5.08
TSTOL	3329.35	3303.11	44.37	-18.12
ΔG_{bind}	-9.98			

Table 5.13. The various components of the Binding Free Energy (kcal/mol) evaluated by Molecular Mechanics-Generalized Borne Surface Area (MM-GBSA) method between SARS-CoV-2 main protease (Mpro)- Rosmanol (ROS) complex.

	Average (Mpro-ROS) (kcal/mol)	Average (Mpro) (kcal/mol)	Average (ROS) (kcal/mol)	Δ (kcal/mol)
VDW	-2349.32	-2316.12	-1.42	-31.77
ELE	-21530.17	-21413.80	-95.14	-21.22
GB	-2709.64	-2698.31	-23.17	11.84
GBSUR	111.81	111.40	3.46	-3.04
GAS	-23879.49	-23729.93	-96.57	-52.99
GBSOL	-2597.82	-2606.91	-19.70	28.79
GBTOT	-26477.32	-26326.84	-116.27	-34.19
TSTRA	17.01	16.99	12.93	-12.92
TSROT	17.72	17.71	10.39	-10.38
TSVIB	3282.50	3257.09	22.23	3.16
TSTOT	3317.22	3291.80	45.56	-20.14
ΔG_{bind}	-14.05			

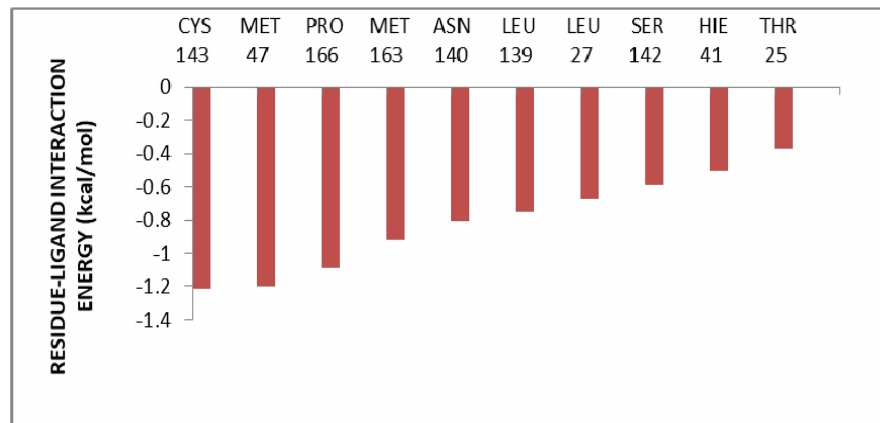
Table 5.14. The various components of the Binding Free Energy (kcal/mol) evaluated by Molecular Mechanics-Poisson-Boltzmann Surface Area (MM-PBSA) method between SARS-CoV-2 main protease (Mpro)- Rosmanol(ROS) complex

	Average (Mpro-ROS) (kcal/mol)	Average (Mpro) (kcal/mol)	Average (ROS) (kcal/mol)	▲ (kcal/mol)
VDW	-2349.32	-2316.12	-1.42	-31.78
ELE	-21530.17	-21413.80	-95.14	-21.23
PB	-2736.89	-2748.61	-25.20	36.92
NPOLAR	2368.27	2405.68	37.97	-75.38
DISPER	-1364.39	-1365.04	-36.80	37.45
GAS	-23879.49	-23729.93	-96.57	-52.99
PBSOL	-1733.01	-1763.97	-24.03	54.98
PBTOL	-25612.51	-25434.90	-120.60	-26.01
TSTRA	17.01	16.99	12.93	-12.92
TSTRO	17.72	17.71	10.39	-10.38
TSVIB	3282.50	3257.09	22.23	3.16
TSTOL	3317.22	3291.80	45.56	-20.14
ΔG_{bind}	-5.87			

5.4.3.6. The decomposition of residue.

The contribution of each individual residue to the binding free energy has been examined in depth to understand the protein-ligand binding mechanism. To construct the residue-ligand interaction spectrum, the binding free energy is decomposed in terms of interacting residue-ligand pairs., shown in **Figure 5.15-5.18**. The method of residue decomposition is particularly useful for explaining the protein-ligand binding mechanism at the atomic level, as well as for analysing the contribution of each individual residue to the binding free energy. The contribution toward binding free energy of several key residue-ligand pairs is split into vdW energy, the sum of electrostatic energy and polar solvation energy, and non-polar solvation energy, according to the analytic result of residue-ligand interaction spectrum. From the analysis, we can see the residues in the binding pocket of SARS-CoV-2 Mpro make a significant contribution to binding free energy.

(A)



(B)

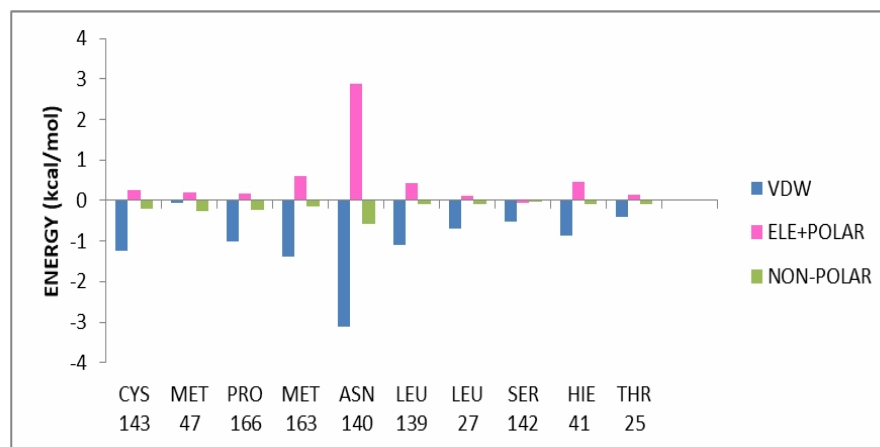


Figure 5.15. Decomposition of the binding free energy on (A) per-residue basis (B) per-residue basis into contribution from vdW energy, the sum of electrostatic energy and polar solvation energy and non-polar solvation energy for SARS-CoV-2 Mpro-Alpha ketoamide complex.

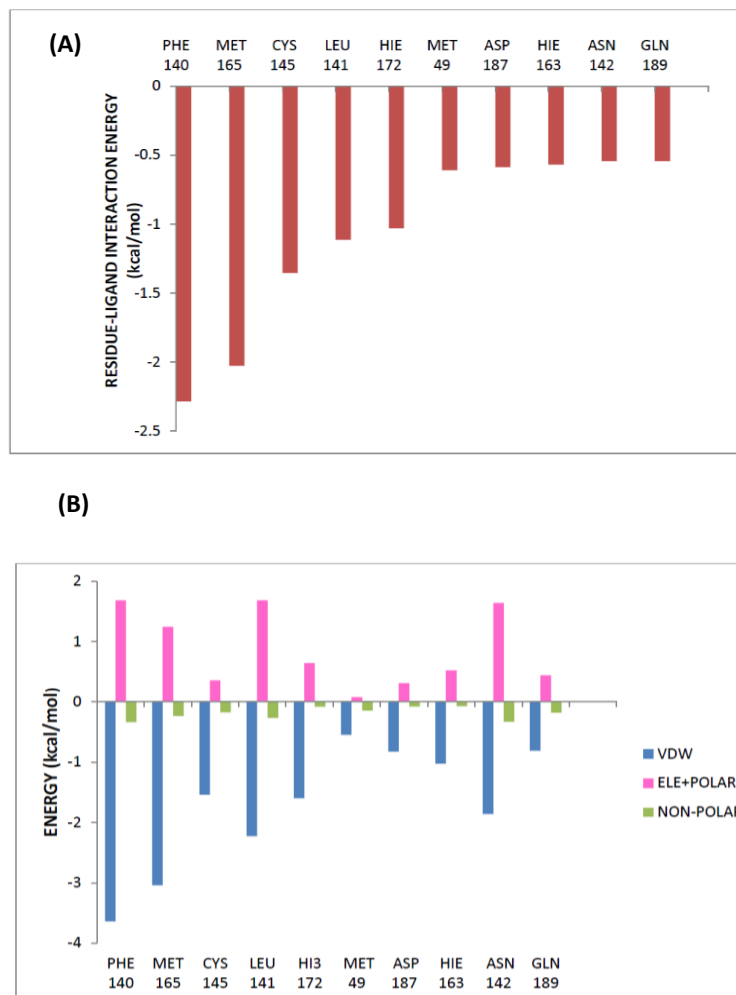


Figure 5.16. Decomposition of the binding free energy on (A) per-residue basis (B) per-residue basis into contribution from vdW energy, the sum of electrostatic energy and polar solvation energy and non-polar solvation energy for SARS-CoV-2 Mpro-Arjunlucoside –I complex

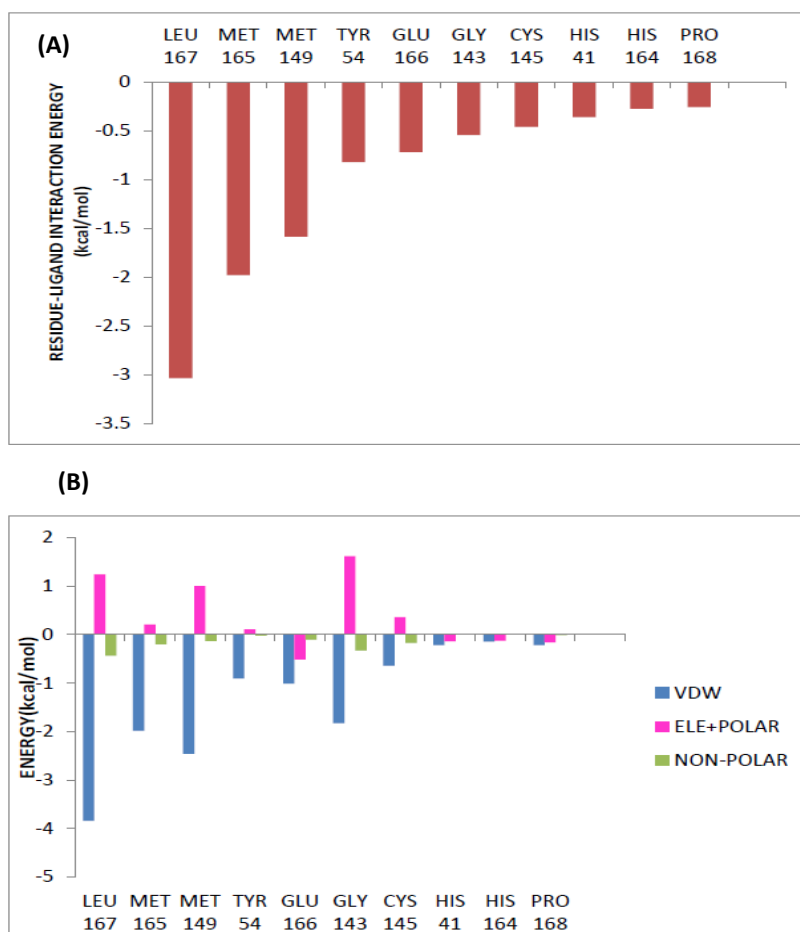


Figure 5.17. Decomposition of the binding free energy on (A) per-residue basis (B) per-residue basis into contribution from vdW energy, the sum of electrostatic energy and polar solvation energy and non-polar solvation energy for SARS-CoV-2 Mpro-Carnosol complex

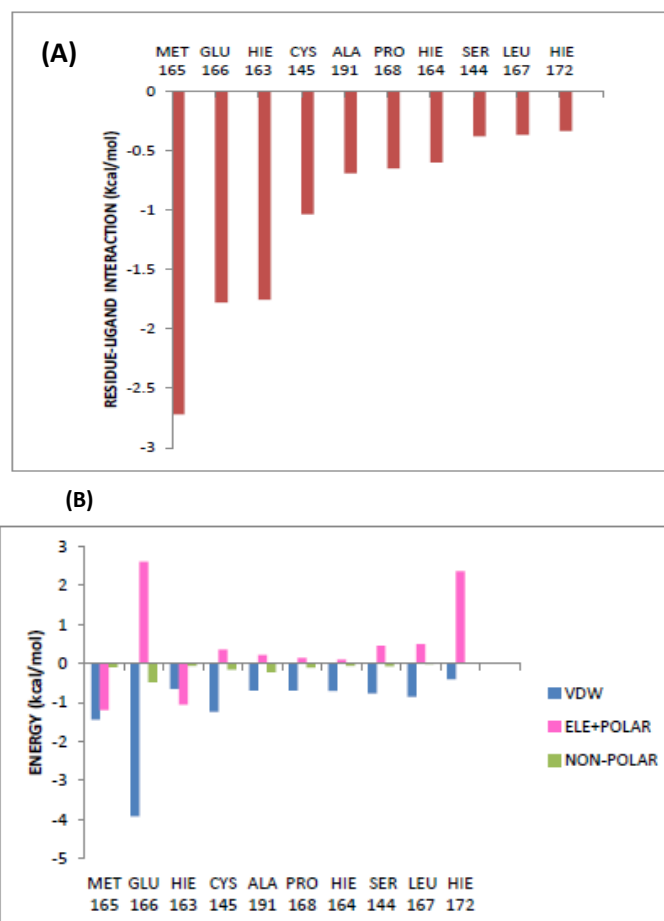


Figure 5.18. Decomposition of the binding free energy on (A) per-residue basis (B) per-residue basis into contribution from vdW energy, the sum of electrostatic energy and polar solvation energy and non-polar solvation energy for SARS-CoV-2 Mpro-Rosmanol complex

5.5. Conclusion:

In this study, we found that small molecule inhibitors (Carnosol, Arjunglucoside-I, and Rosmanol) traced out from Indian spices can act as potential inhibitors of SARS-CoV-2 Mpro. We conducted the research in this direction using in silico approach and our results revealed that Arjunglucoside-I comparatively strongly inhibited the SARS-CoV-2 Mpro followed by Carnosol, Rosmanol and then Alpha-ketoamide (positive control). The PMF calculations revealed that the small molecule inhibitors to have a deeper energy potential depth and consequently a longer residence period (Arjunglucoside-I, Carnosol and Rosmanol) in the binding pocket of SARS-CoV-2 Mpro. The order of inhibition among

the small molecule inhibitors and Alpha-ketoamide (positive control) was determined using binding free energy calculations. ΔG_{bind} for the SARS-CoV-2 Mpro showed the least value for the SARS-CoV-2 Mpro and Arjunglucoside-I complex followed by SARS-CoV-2 Mpro-Carnosol complex, SARS-CoV-2 Mpro-Rosmanol complex and SARS-CoV-2 Mpro-Alpha-ketoamide complex. These findings point to small molecule inhibitors derived from Indian spices as potential SARS-CoV-2 Mpro inhibitors. From the PRED analysis, we found the residues present in the binding pocket of SARS-CoV-2 Mpro provided the highest energy contributions for the SARS-CoV-2 Mpro-small molecules interactions. Our findings shed light on the binding pathway and degree of association between SARS-CoV-2 Mpro and the small molecules (Arjunglucoside-I, Carnosol, and Rosmanol, Alpha-ketoamide (positive control)) in the complex formation. These findings could aid in the development of novel SARS-CoV-2 Mpro inhibitors.

5.6. Bibliography:

- [1]. Cucinotta, D., and Vanelli, M. WHO declares COVID-19 a pandemic. *Acta Biomedica Atenei Parmensis*, 91(1):157-160, 2020. <https://doi.org/10.23750/abm.v91i1.9397>.
- [2]. Touret, F., Gilles, M., Barral, B., Nougairède, A., Decroly, E., Lamballerie, X.D., and Coutard, B. In vitro screening of a FDA approved chemical library reveals potential inhibitors of SARS-CoV-2 replication. *Scientific Reports*, 10(1):13093, 2020. <https://doi.org/10.1038/s41598-020-70143-6>.
- [3]. Kickbusch, I., and Leun, G. Response to the emerging novel coronavirus outbreak. *British Medical Journal*, 368: m406, 2020. <https://doi.org/10.1136/bmj.m406>.
- [4]. Banerjee, A., Kulcsar, K., Misra, V., Frieman, M., and Mossman, K. Bats and coronaviruses. *Viruses*, 11(1): 41, 2019. <https://dx.doi.org/10.3390%2Fv11010041>.
- [5]. Yang, D., and Leibowitz, J.L. The structure and functions of coronavirus genomic 3' and 5' ends. *Virus Research*, 206: 120-33, 2015. <https://doi.org/10.1016/j.virusres.2015.02.025>.
- [6]. Ward, M.P., Li. X., and Tian, K. Novel coronavirus 2019, an emerging public health emergency. *Transboundary and Emerging Diseases*, 67(2): 469-470, 2020. <https://doi.org/10.1111/tbed.13509>.
- [7]. Paules, C.I., Marston, H.D., and Fauci, A.S. Coronavirus Infections-More than Just the Common Cold. *Journal of the American Medical Association*, 323(8): 707-708, 2020. <https://doi.org/10.1001/jama.2020.0757>.

- [8]. Kräusslich, H.G., and Wimmer, E. Viral proteinases. *Annual Review of Biochemistry*, 57: 701-54, 1988. <https://doi.org/10.1146/annurev.bi.57.070188.003413>.
- [9]. Tong, L. Viral proteases. *Annual Review of Biochemistry*, 102(12): 4609-26, 2002. <https://doi.org/10.1021/cr010184f>.
- [10]. Mengist, H.M., Dilnessa, T., and Jin, T. Structural Basis of Potential Inhibitors Targeting SARS-CoV-2 Main Protease. *Frontiers in Chemistry*, 9: 622898, 2021. <https://doi.org/10.3389/fchem.2021.622898>.
- [11]. Citarella, A., Scala, A., Piperno, A., and Micale, N. SARS-CoV-2 Mpro: A Potential Target for Peptidomimetics and Small-Molecule Inhibitors. *Biomolecules*, 11(4), 607, 2021. <https://doi.org/10.3390/biom11040607>.
- [12]. Huff, S., Kummetha, I.R., Tiwari, S.K., Huante, M.B., Clark, A.E., Wang, S., Bray, W., Smith, D., Carlin, A.F., Endsley, M., and Rana, T.M. Discovery and Mechanism of SARS-CoV-2 Main Protease Inhibitors. *Journal of Medicinal Chemistry*, 65(4): 2866-2879, 2022. <https://doi.org/10.1021/acs.jmedchem.1c00566>.
- [13]. Krumm, Z.A., Lloyd, G.M., Francis, C.P., Nasif, L.H., Mitchell, D.A., Golde, T.E., Giasson, B.I., and Xia, Y. Precision therapeutic targets for COVID-19. *Virology Journal*, 18(1): 66, 2021. <https://doi.org/10.1186/s12985-021-01526-y>.
- [14]. Li, J.Q., Gao, H., Zhai, L., Sun, L.Y., Chen, C., Chigan, J.Z., Ding, H.H., and Yang, K.W. Dipyrindyl-substituted thiosemicarbazone as a potent broad-spectrum inhibitor of metallo- β -lactamases. *Bioorganic & Medicinal Chemistry*, 38: 116128, 2021. <https://doi.org/10.1016/j.bmc.2021.116128>.
- [15]. Gossen, J., Albani, S., Hanke, A., Joseph, B.P., Bergh, C., Kuzikov, M., Costanzi, E., Manelfi, C., Storici, P., Gribbon, P., Beccari, A.R., Talarico, C., Spyrikis, F., Lindahl, E., Zaliani, A., Carloni, P., Wade, R.C., Muziani, F., Kokh, D.B., and Rossetti, G. A Blueprint for High Affinity SARS-CoV-2 Mpro Inhibitors from Activity-Based Compound Library Screening Guided by Analysis of Protein Dynamics. *ACS pharmacology & translational science*, 4(3): 1079-1095, 2021. <https://doi.org/10.1021/acsptsci.0c00215>.
- [16]. Sharma, A., Vora, J., Patel, D., Sinha, S., Jha, P.C., and Shrivastava, N. Identification of natural inhibitors against prime targets of SARS-CoV-2 using molecular docking, molecular dynamics simulation and MM-PBSA approaches. *Journal of Biomolecular Structure and Dynamics*, 40(7): 3296-3311, 2022. <https://doi.org/10.1080/07391102.2020.1846624>.
- [17]. Liu, J., Zhu, J., Xue, J., Qin, Z., Shen, F., Liu, J., Chen, X., Li, X., Wu, Z., Xiao, W., Zheng, C., and Wang, Y. In silico-based screen synergistic drug combinations from herb medicines: a case using

- Cistanche tubulosa. *Scientific Reports*, 7(1):16364, 2017. <https://doi.org/10.1038/s41598-017-16571-3>.
- [18]. Rahimi, A., Mirzazadeh, A., and Tavakolpour, S. Genetics and genomics of SARS-CoV-2: A review of the literature with the special focus on genetic diversity and SARS-CoV-2 genome detection. *Genomics*, 113: 1221-1232, 2021. <https://doi.org/10.1016/j.ygeno.2020.09.059>.
- [19]. Zhang, L., Lin, D., Sun, X., Curth, U., Drosten, C., Sauerhering, L., Becker, S., Rox, K., and Hilgenfeld, R. Crystal structure of SARS-CoV-2 main protease provides a basis for design of improved α -ketoamide inhibitors. *Science*, 368(6489): 409-412, 2020. <https://doi.org/10.1126/science.abb3405>.
- [20]. Morse, J.S., Lalonde, T., Xu, S., and Liu, W.R. Learning from the Past: Possible Urgent Prevention and Treatment Options for Severe Acute Respiratory Infections Caused by 2019-nCoV. *Chembiochem*, 21(5):730-738, 2020. <https://doi.org/10.1002/cbic.202000047>.
- [21]. Sk, M.F., Roy, R., and Kar, P. Exploring the potency of currently used drugs against HIV-1 protease of subtype D variant multiscale simulations. *Journal of Biomolecular Structure and Dynamics*, 39(3): 988-1003, 2020. <https://doi.org/10.1080/07391102.2020.1724196>.
- [22]. Cui, W., Yang, K., and Yang, H. Recent Progress in the Drug Development Targeting SARS-CoV-2 Main Protease as Treatment for COVID-19. *Frontiers in Molecular Biosciences*, 7:616341, 2020. <https://doi.org/10.3389/fmolb.2020.616341>.
- [23]. Abdellatiif, M. H., Ali, A., Ali, A., and Hussien, M. Computational studies by molecular docking of some antiviral drugs with COVID-19 receptors are an approach to medication for COVID-19. *Open Chemistry*, 19(1): 245-264, 2021. <https://doi.org/10.1515/chem-2021-0024>.
- [24]. Muralidharan, N., Sakthivel, R., Velmurugan, D., Gromiha, M.M. Computational studies of drug repurposing and synergism of lopinavir, oseltamivir and ritonavir binding with SARS-CoV-2 protease against COVID-19. *Journal of biomolecular structure & dynamics*, 39(7):2673-2678, 2021. <http://doi.org/10.1080/07391102.2020.1752802>.
- [25]. Mongia, A., Saha, S.K., Chouzenoux, E., and Majumdar, A. A computational approach to aid clinicians in selecting antiviral drugs for COVID-19 trials. *Scientific Reports*, 11(1): 9047, 2021. <https://doi.org/10.1038/s41598-021-88153-3>.
- [26]. Behera, S.K., Vhora, N., Contractor, D., Shard, A., Kumar, D., Kalia, K., Jain, A. Computational drug repurposing study elucidating simultaneous inhibition of entry and replication of novel corona virus by Grazoprevir. *Scientific reports*, 2021, 11(1), 7307, <https://doi.org/10.1038/s41598-021-86712-2>.
- [27]. Ibrahim, M.A.A., Abdelrahman, A.H.M., Allemailem, K.S., Almatroudi, A., Moustafa, M.F., and Hegazy, M.E.F. In silico evaluation of prospective anti-COVID-19 drug candidates as potential SARS-CoV-2 main protease inhibitors. *The protein journal*, 40(3): 296–309, 2021.

<https://doi.org/10.1007/s10930-020-09945-6>.

[28]. Singh, S.K., Upadhyay, A.K., and Reddy, M.S. Screening of potent drug inhibitors against SARS-CoV-2 RNA polymerase: an in-silico approach. *Biotech*, 11(2): 93, 2021.

<http://doi.org/10.1007/s13205-020-02610-w>.

[29]. Mahanta, S., Chowdhury, P., Gogoi, N., Goswami, N., Borah, D., Kumar, R., Chetia, D., Borah, P., Buragohain, A.K., and Gogoi, B. Potential antiviral activity of approved repurposed drug against main protease of SARS-CoV-2: in-silico based approach. *Journal of biomolecular structure & dynamics*, 39(10): 3802–3811, 2021. <https://doi.org/10.1080/07391102.2020.1768902>.

[30]. Mittal, L., Kumari, A., Srivastava, M., Singh, M., and Asthana, S. Identification of potential molecules against COVID-19 main protease through structure-guided virtual screening approach. *Journal of biomolecular structure & dynamics*, 39(10): 3662–3680, 2021. <http://doi.org/10.1080/07391102.2020.1768151>.

[31]. Elmaaty, A.A., Darwish, K.M., Khattab, M., Elhady, S.S., Salah, M., Hamed, M.I.A., Al-Karmalawy, A.A., and Saleh, M.M. In a search for potential drug candidates for combating COVID-19: computational study revealed salvianolic acid B as a potential therapeutic targeting 3CLpro and spike proteins. *Journal of biomolecular structure & dynamics*, 40(19): 8866–8893, 2021. <https://doi.org/10.1080/07391102.2021.1918256>.

[32]. Al-Karmalawy, A., Dahab, M., Metwaly, A., Elhadi, S.S., Elkaeed, E.B., Eissa, I.H., and Darwish, K.M. Molecular docking and dynamics simulations reveal the potential of anti-HCV drugs to inhibit COVID-19 main protease. *Frontiers in Chemistry*, 9: 661230, 2021, <https://doi.org/10.3389/fchem.2021.661230>.

[33]. Nabi, F., Ahmad, O., Khan, Y.A., Nabi, A., Amiruddin, H.M., Qais, F.A., Masroor, A., Hisamuddin, M., Uversky, V.N., and Khan, R.H. Computational studies on phylogeny and drug designing using molecular simulations for COVID-19. *Journal of biomolecular structure & dynamics*, 40(21): 10753–10762, 2021. <https://doi.org/10.1080/07391102.2021.1947895>

[34]. Umesh, Kundu, D., Selvaraj, C., Singh, S.K., and Dubey, V.K. Identification of new anti-nCoV drug chemical compounds from Indian spices exploiting SARS-CoV-2 main protease as target. *Journal of biomolecular structure & dynamics*, 39(9): 3428–3434, 2021. <https://doi.org/10.1080/07391102.2020.1763202>.

[35]. Cui, W., Yang, K., and Yang, H. Recent Progress in the Drug Development Targeting SARS-CoV-2 Main Protease as Treatment for COVID-19. *Frontiers in molecular biosciences*, 7: 616341, 2020. <https://doi.org/10.3389/fmolb.2020.616341>.

- [36]. Alsamri, H., Hasasna, H.E., Baby, B., Alneyadi, A., Dhaheri, Y.A., Ayoub, M.A., Eid, A.H., Vijayan, R., and Iratni, R. Carnosol Is a Novel Inhibitor of p300 Acetyltransferase in Breast Cancer. *Frontiers in oncology*, 11: 664403, 2021. <https://doi.org/10.3389/fonc.2021.664403>.
- [37]. Lo, A.H., Liang, Y.C., Shiau, S.Y.L., Ho, C.T., and Lin, J.K. Carnosol, an antioxidant in rosemary, suppresses inducible nitric oxide synthase through down-regulating nuclear factor- κ B in mouse macrophages. *Carcinogenesis*, 23(6): 983–991, 2002, <https://doi.org/10.1093/carcin/23.6.983>.
- [38]. Berman, H.M., Westbrook, J., Feng, Z., Gilliland, G., Bhat, T.N., Weissig, H., Shindyalov, I.N., and Bourne, P.E. The protein data bank. *Nucleic acids research*, 28(1): 235–242, 2000. <https://doi.org/10.1093/nar/28.1.235>.
- [39]. Schneidman-Duhovny D, Inbar Y, Nussinov R, and Wolfson HJ. PatchDock and SymmDock: servers for rigid and symmetric docking. *Nucleic acids research*, 33: W363–W367, 2005. <https://doi.org/10.1093/nar/gki481>
- [40]. Connolly, M.L. Analytical molecular surface calculation. *Journal of Applied Crystallography*, 16: 548–558, 1983. <https://doi.org/10.1107/S0021889883010985>
- [41]. Connolly M.L. Solvent-accessible surfaces of proteins and nucleic acids, *Science*, 221(4612): 709–713, 1983. <https://doi.org/10.1126/science.6879170>.
- [42]. Pettersen, E.F., Goddard, T.D., Huang, C.C., Couch, G.S., Greenblatt, D.M., Meng, E.C., and Ferrin, T.E. UCSF Chimera? A visualization system for exploratory research and analysis. *Journal of computational chemistry*, 25(13): 1605–1612, 2004. <https://doi.org/10.1002/jcc.20084>.
- [43]. Jorgensen, W.L., Chandrasekhar, J., Madura, J.D., Impey, R.W., and Klein, M.L. Comparison of simple potential functions for simulating liquid water. *The Journal of Chemical Physics*, 79 (2): 926–935, 1983. <http://dx.doi.org/10.1063/1.445869>.
- [44]. Darden, T., York, D., and Pedersen, L. Particle mesh Ewald: An $N \cdot \log(N)$ method for Ewald sums in large systems. *The Journal of Chemical Physics*, 98 (12): 10089–10092, 1993. <https://doi.org/10.1063/1.464397>.
- [45]. Salomon-Ferrer, R., Gotz, A.W., Poole, D., Le Grand, S., and Walker, R.C. Routine microsecond molecular dynamics simulations with AMBER on GPUs. 2. Explicit solvent particle mesh Ewald. *Journal of chemical theory and computation*, 9(9): 3878–3888, 2013. <https://doi.org/10.1021/ct400314y>.
- [46]. Ryckaert, J.P., Ciccotti, G., and Berendsen, H.J.C. Numerical integration of the cartesian equations of motion of a system with constraints: molecular dynamics of n-alkanes. *Journal of Computational Physics*, 23: 327–341, 1977. [https://doi.org/10.1016/0021-9991\(77\)90098-5](https://doi.org/10.1016/0021-9991(77)90098-5).

- [47]. Berendsen, H.J., Postma, J.V., Van, G.W.F., DiNola, A.R.H.J., and Haak, J.R. Molecular dynamics with coupling to an external bath. *The Journal of Chemical Physics*, 81(8): 3684–3690, 1984. <https://doi.org/10.1063/1.448118>.
- [48]. Roux, B. The calculation of the potential of mean force using computer simulations. *Computer Physics Communications*, 91(1): 275–282, 1995. [https://doi.org/10.1016/0010-4655\(95\)00053-I](https://doi.org/10.1016/0010-4655(95)00053-I).
- [49]. Kumar, S., Rosenberg, J.M., Bouzida, D., Swendsen, R.H., and Kollman, P.A. The weighted histogram analysis method for free energy calculations on biomolecules. I. *Journal of Computational Chemistry*, 13: 1011–1021, 1992, <https://doi.org/10.1002/jcc.540130812>.
- [50]. Souaille, M., and Roux, B. Extension to the weighted histogram analysis method: combining umbrella sampling with free energy calculations. *Computer Physics Communications*, 135: 40–57, 2001. [https://doi.org/10.1016/s00104655\(00\)00215-0](https://doi.org/10.1016/s00104655(00)00215-0)
- [51]. Roe, D.R., and Cheatham III, T.E. PTRAJ and CPPTRAJ: software for processing and analysis of molecular dynamics trajectory data. *Journal of chemical theory and computation*, 9(7): 3084–3095, 2013. <https://doi.org/10.1021/ct400341p>.
- [52]. Miller III, B.R., McGee Jr, T.D., Swails, J.M., Homeyer, N., Gohlke, H., and Roitberg, A.E. MMPBSA.py: an efficient program for end-state free energy calculations. *Journal of chemical theory and computation*, 8(9): 3314–3321, 2012. <https://doi.org/10.1021/ct300418h>.
- [53]. Chen, F., Liu, H., Sun, H., Pan, P., Li, Y., Li, D., and Hou, T. Assessing the performance of the MM/PBSA and MM/GBSA methods. 6. Capability to predict protein–protein binding free energies and re-rank binding poses generated by protein–protein docking. *Physical Chemistry Chemical Physics*, 18(32): 22129–22139, 2016, <https://doi.org/10.1039/c6cp03670h>.
- [54]. Genheden, S., and Ryde, U. The MM/PBSA and MM/GBSA methods to estimate ligand-binding affinities. *Expert opinion on drug discovery*, 10(5): 449–461, 2015. <http://doi.org/10.1517/17460441.2015.1032936>.
- [55]. Case, D.A. Normal mode analysis of protein dynamics. *Current opinion in structural biology*, 4(2): 285–290, 1994. [https://doi.org/10.1016/S0959-440X\(94\)90321-2](https://doi.org/10.1016/S0959-440X(94)90321-2).
- [56]. Karplus, M., and Kushick, J.N. Method for estimating the configurational entropy of macromolecules. *Macromolecules*, 14(2): 325–332, 1981. <https://doi.org/10.1021/ma50003a019>.
- [57]. Chen, J., Yin, B., Pang, L., Wang, W., Zhang, J.Z., and Zhu, T. Binding modes and conformational changes of FK506 binding protein 51 induced by inhibitor bindings: insight into molecular mechanisms based on multiple simulation technologies. *Journal of biomolecular structure & dynamics*, 38(7), 2141–2155, 2020. <https://doi.org/10.1080/07391102.2019.1624616>.

- [58]. Gao, J., Wang, Y., Chen, Q., and Yao, R. Integrating molecular dynamics simulation and molecular mechanics/generalized Born surface area calculation into pharmacophore modeling: a case study on the proviral integration site for Moloney murine leukemia virus (Pim)-1 kinase inhibitors. *Journal of Biomolecular Structure and Dynamics*, 38: 1-10, 2020. <http://doi.org/10.1080/07391102.2019.1571946>.
- [59]. Joshi, T., Joshi, T., Sharma, P., Chandra, S., and Pande, V. Molecular docking and molecular dynamics simulation approach to screen natural compounds for inhibition of *Xanthomonas oryzae* pv. *Oryzae* by targeting Peptide Deformylase. *Journal of biomolecular structure & dynamics*, 39(3): 823–840, 2021. <https://doi.org/10.1080/07391102.2020.1719200>.
- [60]. Sun, H., Duan, L., Chen, F., Liu, H., Wang, Z., Pan, P., Zhu, F., Zhang, J.Z.H., and Hou, T. Assessing the performance of MM/PBSA and MM/GBSA methods. 7. Entropy effects on the performance of endpoint binding free energy calculation approaches. *Physical Chemistry Chemical Physics*, 20(21): 14450-14460, 2018. <https://doi.org/10.1039/C7CP07623A>.
- [61]. Wang, E., Sun, H., Wang, J., Wang, Z., Liu, H., Zhang, J.Z.H., and Hou, T. End-Point Binding Free Energy Calculation with MM/PBSA and MM/GBSA: Strategies and Applications in Drug Design. *Chemical Reviews*, 119(16): 9478-9508, 2019. <https://doi.org/10.1021/acs.chemrev.9b00055>.
- [62]. Zhang, W., Yang, F., Ou, D., Lin, G., Huang, A., Liu, N., and Li, P. Prediction, docking study and molecular simulation of 3D DNA aptamers to their targets of endocrine disrupting chemicals. *Journal of biomolecular structure & dynamics*, 37(16): 4274–4282, 2019. <https://doi.org/10.1080/07391102.2018.1547222>.
- [63]. Sun, H., Tian, S., Zhou, S., Li, Y., Li, D., Xu, L., Shen, M., Pan, P., and Hou, T. Revealing the favorable dissociation pathway of type II kinase inhibitors via enhanced sampling simulations and two-end-state calculations. *Scientific reports*, 5, 8457, 2015. <https://doi.org/10.1038/srep08457>.